The Astrophysical Journal, 941:107 (30pp), 2022 December 20 https://doi.org/10.3847/1538-4357/ac9842

Luminous Supernovae: Unveiling a Population between Superluminous and Normal Core-collapse Supernovae

Sebastian Gomez[1,2], Edo Berger[2], Matt Nicholl[3], Peter K. Blanchard[4], and Griffin Hosseinzadeh[5]
[1] Space Telescope Science Institute, 3700 San Martin Drive, Baltimore, MD 21218, USA; sgomez@stsci.edu
[2] Center for Astrophysics | Harvard & Smithsonian, 60 Garden Street, Cambridge, MA 02138-1516, USA
[3] Birmingham Institute for Gravitational Wave Astronomy and School of Physics and Astronomy, University of Birmingham, Birmingham B15 2TT, UK
[4] Center for Interdisciplinary Exploration and Research in Astrophysics and Department of Physics and Astronomy, Northwestern University, 1800 Sherman Avenue, 8th Floor, Evanston, IL 60201, USA
[5] Steward Observatory, University of Arizona, 933 North Cherry Avenue, Tucson, AZ 85721, USA
Received 2022 April 18; revised 2022 September 11; accepted 2022 October 4; published 2022 December 15

Abstract

Stripped-envelope core-collapse supernovae can be divided into two broad classes: the common Type Ib/c supernovae (SNe Ib/c), powered by the radioactive decay of ^{56}Ni, and the rare superluminous supernovae (SLSNe), most likely powered by the spin-down of a magnetar central engine. Up to now, the intermediate regime between these two populations has remained mostly unexplored. Here, we present a comprehensive study of 40 *luminous supernovae* (LSNe), SNe with peak magnitudes of $M_r = -19$ to -20 mag, bound by SLSNe on the bright end and by SNe Ib/c on the dim end. Spectroscopically, LSNe appear to form a continuum between Type Ic SNe and SLSNe. Given their intermediate nature, we model the light curves of all LSNe using a combined magnetar plus radioactive decay model and find that they are indeed intermediate, not only in terms of their peak luminosity and spectra, but also in their rise times, power sources, and physical parameters. We subclassify LSNe into distinct groups that are either as fast evolving as SNe Ib/c or as slow evolving as SLSNe, and appear to be either radioactively or magnetar powered, respectively. Our findings indicate that LSNe are powered by either an overabundant production of ^{56}Ni or by weak magnetar engines, and may serve as the missing link between the two populations.

Unified Astronomy Thesaurus concepts: Astronomical methods (1043); Surveys (1671); Supernovae (1668); Core-collapse supernovae (304)

Supporting material: figure sets, machine-readable tables

1. Introduction

Stars more massive than $\sim 8\ M_\odot$ end their lives in a core-collapse supernova (CCSN). Some of these massive stars lose their hydrogen and/or helium envelopes before explosion, either through winds or interaction with a binary companion (e.g., Heger et al. 2003; Smith 2014). These stripped stars can lead to either Type Ib SNe (lacking hydrogen), or Type Ic SNe (lacking hydrogen and helium) (Woosley et al. 1995; Filippenko 1997). Based on their light-curve evolution and spectral properties, we know SNe Ib/c are powered by the radioactive decay of ^{56}Ni synthesized during the explosion (Arnett 1982; Gal-Yam 2017). SNe Ib/c are relatively dim and fast evolving, reaching typical peak magnitudes of $M_r = -17.7 \pm 0.9$ within about 20 ± 10 days after explosion (Barbarino et al. 2020). Spectroscopically, SNe Ib/c exhibit strong suppression blueward of $\sim$4000 Å due to line blanketing from Fe-peak elements. In terms of their environments, SNe Ib/c tend to occur in galaxies with relatively high metallicities of $12+\log(\mathrm{O/H}) = 8.8 \pm 0.3$ (Modjaz et al. 2020).

More recently, a new class of stripped-envelope CCSN was discovered and designated Type I superluminous supernovae (hereafter, SLSNe; Chomiuk et al. 2011; Quimby et al. 2011). SLSNe can be up to 100 times more luminous than SNe Ib/c and reach typical peak magnitudes of $M_r = -21.7 \pm 0.7$ (e.g., Gal-Yam 2019; Gomez et al. 2020a; Chen et al. 2022) with longer rise times of $\sim$20–80 days (Nicholl et al. 2017). The spectra of SLSNe are marked by distinctive W-shaped O II absorption features around $\sim$3500–5000 Å at early times (Chomiuk et al. 2011; Quimby et al. 2011); and while the spectra of SLSNe tend to be much bluer than those of SNe Ib/c before peak, as they evolve and cool they begin to more closely resemble normal SNe Ic (e.g., Pastorello et al. 2010; Quimby et al. 2018; Blanchard et al. 2019; Nicholl et al. 2019). Unlike SNe Ib/c, SLSNe generally occur in low-metallicity galaxies with typical values of $12+\log(\mathrm{O/H}) = 8.4 \pm 0.3$ (Lunnan et al. 2014). Their blue spectra, bright and slowly evolving light curves, and low-metallicity environments all point to an energy source distinct from radioactive decay (Angus et al. 2016; Nicholl et al. 2017; Margalit et al. 2018), most likely the spin-down energy of a millisecond magnetar born in the explosion (Kasen & Bildsten 2010; Woosley 2010). Additionally, it has been shown that SLSNe progenitors are generally more massive before explosion ($\approx$3–40 $M_\odot$; Blanchard et al. 2020) than those of SNe Ib/c ($4.5 \pm 0.8\ M_\odot$; Barbarino et al. 2020). SLSNe are also rare, representing $\lesssim$1% of the SNe Ib/c volumetric rate (Frohmaier et al. 2021).

Given the distinct energy sources of SNe Ib/c and SLSNe, we may expect SNe in the intermediate regime to exist. Some studies have begun exploring these intermediate SNe, such as SN 2012aa (Roy et al. 2016) or SNe 2019dwa, 2019cri, 2019hge, and 2019unb (Prentice et al. 2021), which along with De Cia et al. (2018), have shown that the distribution of peak magnitudes from SNe Ib/c to SLSNe appears to be continuous.

While several models exist to explain the additionally luminosity in SNe beyond radioactive decay, such as circumstellar interaction (e.g., Chevalier & Irwin 2011; Chatzopoulos et al. 2013) or the pulsational-pair instability phenomenon (e.g., Woosley et al. 2007; Gomez et al. 2019), here, we focus on the magnetar central engine model, the leading theory for the power source behind SLSNe (e.g., Mazzali et al. 2016; Nicholl et al. 2017; Hsu et al. 2021; Könyves-Tóth & Vinkó 2021; Chen et al. 2022; Liu et al. 2022). Anderson (2019) showed that the peak luminosities of observed SNe Ib/c are brighter than what is expected from radioactive decay models alone. Ertl et al. (2020) reach a similar conclusion and argued that an additional contribution from a magnetar central engine in SNe Ib/c might be responsible for the missing luminosity.

One possibility is that these intermediate SNe could be powered by either weaker magnetar engines than those of normal SLSNe, or an overabundant production of ^{56}Ni compared to SNe Ib/c. Milisavljevic et al. (2013) studied SN 2012au in an effort to link SNe Ib/c to SLSNe and suggested that either CSM interaction, a pair-instability explosion, or a magnetar central engine might be viable power sources to unify the models of stripped-envelope CCSN. Alternatively, Mazzali et al. (2014) suggest that a fraction of the total energy from magnetars emerges in the form of a focused relativistic jet, adding energy to the SN, similar to the jet-driven process that Soker & Gilkis (2017) suggest power SLSNe. Mazzali et al. (2014) also point out that all known SNe with corresponding gamma-ray bursts (GRBs) are luminous, and suggested that all GRBs associated with *luminous supernovae* (LSNe) are produced by magnetars, while the GRBs that result from collapsars may not produce LSNe. While no SLSNe have been confirmed to be associated with GRBs, Lunnan et al. (2014) suggest that the similar host galaxies between SLSNe and GRBs might imply a connection and a common power source, which agrees with the models of Metzger et al. (2015), who suggest that magnetars are likely to be the central engine powering both long GRBs and SLSNe.

Here, we report the first systematic search and analysis of such intermediate events, their properties, and power sources. We present a list of 40 SNe with intermediate luminosities between SLSNe and SNe Ib/c, compiled either through our own observational program, or publicly available transients from the literature. We define the sample of LSNe as SNe with spectra consistent with a stripped-envelope CCSN and a peak absolute r-band magnitude of $M_r = -19$ to $M_r = -20$ mag, bound by SLSNe on the bright end and by SNe Ib/c on the dim end. We caution that the LSN label does not necessarily imply a physical connection between these objects, but is rather a phenomenological grouping based solely on their peak luminosity. We use these selection criteria to explore their physical properties, connections to both SLSNe and SNe Ib/c, and subgroupings within the LSNe sample.

This paper is structured as follows: In Section 2, we present the samples of LSNe, SNe Ib/c, and SLSNe used in our analysis, as well as the sources of their photometry and spectroscopy. In Section 3, we describe the light-curve modeling, and in Section 4, we discuss the results of these models. In Section 5, we outline the possible subgroupings for LSNe. In Section 6, we discuss the observational features and rates of the LSNe population, and finally conclude in Section 7. Throughout this paper, we assume a flat Lambda cold dark matter cosmology with $H_0 = 69.3$ km s^{-1} Mpc^{-1}, $\Omega_m = 0.286$, and $\Omega_\Lambda = 0.712$ (Hinshaw et al. 2013).

2. Sample of LSNe

We begin our analysis by gathering a sample of 315 stripped-envelope core-collapse supernovae (CCSNe), including a list of all known SLSNe in addition to SNe Ib/c and SNe Ic-BL with above-average luminosities, and a sample of SNe Ic/Ic-BL for comparison. The SNe in this master list were obtained either from the Open Supernova Catalog[6] (OSC; Guillochon et al. 2017), the Transient Name Server (TNS),[7] the Weizmann Interactive Supernova Data Repository (WISeREP; Yaron & Gal-Yam 2012),[8] a literature search, or from our own FLEET transient follow-up program (Gomez et al. 2020b). We include comparison samples of SNe Ic-BL from Taddia et al. (2019), SNe Ic from Barbarino et al. (2020), and SLSNe from S. Gomez et al. (2022, in preparation), where a full description of the SLSNe sample will be presented in a forthcoming paper. In total, we include 149 SLSNe and 61 SNe Ic/Ic-BL for our comparative analysis. The individual SNe used for this work are all listed in Appendix A.

We select the LSNe from our master sample by focusing on the objects that have a peak absolute magnitude of $M_r = -19$ to -20 mag. For SNe that either do not have r-band observations available, or that were not observed during peak, we estimate their peak absolute magnitude using the light-curve models discussed in Section 3. This range is motivated by the fact that SNe brighter than $M_r \approx -20$ mag tend to show relatively uniform spectroscopic and photometric features that allow us to classify them as SLSNe, and SNe dimmer than $M_r \approx -19$ mag can usually be confidently classified as SNe Ib/c.

Our final sample is made up of 59 LSNe, in addition to the 149 SLSNe and 61 SNe Ic/Ic-BL used for comparison. These SNe are not easily classified into either the SLSNe or SNe Ib/c categories, but lie somewhere in an intermediate regime in terms of both their light curves and spectra. Of these 59 LSNe, we designate 25 as "Gold" LSNe, when we have both enough photometry to be able to model their light curves, and spectroscopic observations from which we can verify their classification as stripped-envelope CCSNe. We designate 15 objects as "Silver" when either their spectroscopic data is of poor quality but still consistent with stripped-envelope CCSNe, or they lack good photometric coverage before peak, but we are still able to constrain their peak using light-curve models. Lastly, we label 19 objects as "Bronze" LSNe when either they do not have photometry available near peak, have less than four epochs of photometry, or have no public spectra available, any of which prevents us from producing trustworthy light-curve models and/or confident spectroscopic classifications. We do not include the Bronze LSNe in our analysis. The full list of 59 LSNe, along with their individual data sources, notes, and peculiarities are presented in Appendix A. The final working sample of 40 Gold and Silver LSNe is listed in Table 1.

2.1. Photometry

We collect all available photometry for the 315 SNe in our sample. We obtain publicly available photometry from the OSC, TNS, and WISeREP for the SNe that have these data

[6] https://sne.space/; frontend now defunct, but backend available.
[7] https://www.wis-tns.org/
[8] https://www.wiserep.org/

Table 1
LSNe

Name	Redshift	Literature Class.	Spectral Group	Light Curve	Quality
DES14C1rhg	0.481	SLSN-I	Superluminous	Fast	Gold
DES15C3hav	0.392	SLSN-I	Superluminous	Fast	Gold
DES16C3cv	0.727	SLSN-I	Normal	Slow	Gold
iPTF13dnt	0.137	Ic-BL	Normal	Fast	Silver
iPTF16asu	0.187	SLSN-I	Superluminous	Fast	Gold
iPTF17cw	0.093	Ic-BL	Normal	Fast	Gold
OGLE15xl	0.198	SLSN-I	Superluminous	Slow	Silver
PS15cvn	0.058	Ic-BL	Normal	Fast	Gold
PTF10gvb	0.098	Ic-BL	Normal	Fast	Gold
PTF10iam	0.109	SLSN-I/Ic	Superluminous	Medium	Silver
PTF11img	0.158	Ic-BL	Normal	Fast	Gold
PTF12gty	0.177	SLSN-I/Ic	Superluminous	Slow	Gold
PTF12hni	0.106	SLSN-I	Ambiguous	Medium	Gold
SN 1991D	0.042	Ib	Ambiguous	Fast	Silver
SN 2003L	0.021	Ib/c	Normal	Slow	Silver
SN 2007ce	0.046	Ic-BL	Normal	Fast	Silver
SN 2009cb	0.187	SLSN-I	Superluminous	Fast	Silver
SN 2010ay	0.067	Ic-BL	Normal	Fast	Silver
SN 2011kl	0.677	SLSN-I/GRB	Superluminous	Fast	Gold
SN 2012aa	0.083	SLSN-I/Ibc	Ambiguous	Slow	Gold
SN 2013hy	0.663	SLSN-I	Superluminous	Medium	Silver
SN 2018beh	0.060	Ib/Ic	Superluminous	Slow	Gold
SN 2018don	0.073	SLSN-I/Ic	Superluminous	Slow	Silver
SN 2018fcg	0.101	SLSN-I	Normal	Fast	Gold
SN 2019cri	0.050	Ic	Normal	Slow	Gold
SN 2019dwa	0.082	Ic	Ambiguous	Medium	Gold
SN 2019gam	0.124	SLSN-Ib/IIb	Superluminous	Slow	Silver
SN 2019hge	0.086	SLSN-Ib	Superluminous	Slow	Gold
SN 2019J	0.120	SLSN-I	Superluminous	Slow	Gold
SN 2019moc	0.056	Ic	Normal	Fast	Gold
SN 2019obk	0.166	SLSN-Ib	Superluminous	Slow	Silver
SN 2019pvs	0.167	SLSN-I	Superluminous	Slow	Gold
SN 2019stc	0.117	Ic	Normal	Slow	Gold
SN 2019unb	0.064	SLSN-Ib	Superluminous	Slow	Gold
SN 2019uq	0.100	Ic	Normal	Fast	Silver
SN 2019wpb	0.068	Ic	Normal	Fast	Silver
SN 2021lei	0.112	Ic	Normal	Fast	Silver
SN 2021lwz	0.065	SLSN-I	Superluminous	Fast	Gold
SN 2021uvy	0.095	SLSN-I/Ib/c	Normal	Slow	Gold
SN 2021ybf	0.130	SLSN-I	Normal	Slow	Gold

Note. List of all the Gold and Silver LSNe used for this work, sorted alphabetically. We include classifications from the literature for each object from references listed in Appendix A, in addition to our own label based solely on their spectral features as either "Superluminous" for SLSNe-like events or "Normal" for SNe Ic/Ic-BL-like events. We add a light-curve classification based on the duration of the light-curve rise and whether it is fast like SNe Ic ($\lesssim$25 days), slow like SLSNe ($\gtrsim$35 days), or intermediate. Additional Bronze objects are listed in Appendix A but are otherwise excluded from this work.

available. In addition, we include photometry from the Zwicky Transient Facility (ZTF; Bellm et al. 2019) taken from the Automatic Learning for the Rapid Classification of Events (ALeRCE) broker (Förster et al. 2021), the Asteroid Terrestrial-impact Last Alert System (ATLAS; Tonry et al. 2018), the All Sky Automated Survey for SuperNovae (ASAS-SN; Kochanek et al. 2017), the Gaia Science Alerts (GSA; Wyrzykowski 2016), the Optical Gravitational Lensing Experiment (OGLE; Wyrzykowski et al. 2014), the Catalina Real Time Transient Survey (CRTS; Drake et al. 2009), and the Pan-STARRS Survey for Transients (PSST; Huber et al. 2015). Photometry from ZTF, ATLAS, PSST, and ASAS-SN is reported from difference images and therefore already has the host flux subtracted. Photometry from the GSA, CRTS, and OGLE does not have the host contribution subtracted, so we subtract the corresponding host magnitude whenever necessary and possible.

In addition to publicly available photometry, we perform our own photometry on either public images or images from our own FLEET transient follow-up program (Gomez et al. 2020a). A few SNe observed by ZTF had sparsely sampled light curves reported by the automatic photometry pipeline. For these SNe, we download the raw ZTF images from the NASA/IPAC Infrared Science Archive[9] to redo the photometry and recover any subthreshold detections that were missed by the automated pipeline. Additionally, we include *gri* images of SNe that were observed by the Global Supernova Project (GSP) with the Las Cumbres Observatory Global Telescope Network (LCO; Brown et al. 2013). Finally, we include images taken as

[9] https://irsa.ipac.caltech.edu/Missions/ztf.html

part of FLEET with either KeplerCam on the 1.2 m telescope at the Fred Lawrence Whipple Observatory (FLWO), the Low Dispersion Survey Spectrograph (LDSS3c; Stevenson et al. 2016) or Inamori-Magellan Areal Camera and Spectrograph (IMACS; Dressler et al. 2011) both on the Magellan Clay 6.5 m telescopes at Las Campanas Observatory, or Binospec (Fabricant et al. 2019) on the MMT 6.5 m telescope.

We perform photometry on all images from ZTF, LCO, and FLEET in the same manner. Instrumental magnitudes are measured by modeling the point-spread function (PSF) of each image using field stars and subtracting the model PSF from the target. The magnitudes are then calibrated to AB magnitudes from the PS1/3π catalog (Chambers et al. 2016). For the majority of sources, we separate the flux of the SN from its host galaxy by performing difference imaging using a pre-explosion PS1/3π template for comparison. We subtract the template from the science images using `HOTPANTS` (Becker 2015). For sources where there is no host galaxy detected above the PS1/3π detection limit of $\approx$23 mag, we report PSF photometry taken directly from the science images without subtracting a template. The details for the data reduction of each SN are listed in Appendix A.

Finally, we verify that all the photometry is either already corrected for Galactic extinction, or correct it directly. We use the dust maps from Schlafly & Finkbeiner (2011) to obtain an estimate of $E(B-V)$ and the Barbary (2016) implementation of the Cardelli et al. (1989) extinction law to calculate the corresponding extinction in each band.

A plot showing the *r*-band light curves of all 40 Gold and Silver LSNe is shown in Figure 1. The blue and red-shaded regions in Figure 1 represent the 1σ, 2σ, and 3σ intervals for the light curves of SLSNe and SNe Ic, respectively. These regions were estimated by averaging the light-curve models of all the SLSNe and SNe Ic/Ic-BL used for our comparative analysis, the full list of SNe is listed in Appendix F.

2.2. Spectra

In this work, we focus on the photometric properties of LSNe, but for comparison and to verify their classification as stripped-envelope CCSNe, we make use of either publicly available optical spectra, or our own newly collected spectra. The public spectra were obtained from WISeREP, the OSC, or the TNS. Some spectra were also obtained from published papers, either from journal databases or private communication with the authors. We use these public spectra to verify the classification given to each SN. Special care is taken for objects that have only been classified in an Astronomer's Telegram or TNS report, but not in a refereed publication. We then verify the redshift of each SN and update it if a better estimate was found from newer or higher quality spectra. Finally, we correct these spectra for Galactic extinction using the extinction maps from Schlafly & Finkbeiner (2011) and the Barbary (2016) implementation of the Cardelli et al. (1989) extinction law. The individual data sources and any notes regarding the spectra of each SN are listed in Appendix A.

The newly collected spectra presented here are part of our FLEET observational program. These spectra were taken with either LDSS3c, Binospec, IMACS, or the Blue Channel spectrographs (Schmidt et al. 1989) on the MMT 6.5 m telescope. We reduced these spectra using standard IRAF routines with the `twodspec` package. The spectra were bias subtracted and flat fielded, the sky background was modeled and subtracted from each image, and the one-dimensional spectra were optimally extracted, and weighed by the inverse variance of the data. Wavelength calibration was applied using an arc lamp spectrum taken near the time of each science image. Relative flux calibration was applied to each spectrum using a standard star taken close to the time of observation. Lastly, the spectra were corrected for Galactic extinction in the same way as the public spectra described above.

Spectroscopically, LSNe are not a uniform sample but span a wide range of features. Some LSNe are blue like SLSNe, while others are red and closely resemble SNe Ic. Representative spectra of LSNe are shown in Figure 2, where we include the closest spectrum to peak for each LSN that has a spectrum taken within $\pm$10 days of peak. We find that LSNe appear to create a smooth continuum, from blue and SLSN-like to red and SN Ic-like, without a clear threshold or distinction that allows us to separate them neatly into either class. An in-depth study of the spectral properties of LSNe will be presented in a future paper. All spectroscopy used for this work is made available on WISeREP[10] (Yaron & Gal-Yam 2012).

3. Light-curve Modeling

To explore the properties of LSNe, and to enable a robust comparison to SLSNe and SNe Ic/Ic-BL, we model the light curves of all the LSNe, SLSNe, and SNe Ic/Ic-BL in our sample in a uniform way. To achieve this we use the Modular Open-Source Fitter for Transients (`MOSFiT`) package, a flexible Python code that uses the `emcee` (Foreman-Mackey et al. 2013) Markov chain Monte Carlo (MCMC) implementation to fit the light curves of transients using a variety of different power sources (Guillochon et al. 2018). Since SNe Ic/Ic-BL are known to be powered by radioactive decay (Filippenko 1997; Taddia et al. 2019), and SLSNe are likely powered by a magnetar central engine (Kasen & Bildsten 2010; Woosley 2010; Nicholl et al. 2017), we model all light curves using a combined magnetar central engine plus radioactive decay model (designated `slsnni`). By fitting all SNe with the same model we can evaluate which power source best reproduces their light curves, without imposing our own assumption based on properties such as peak magnitude or spectral classification. We test for convergence by ensuring that the models reach a potential scale reduction factor of $<$1.3 (Gelman & Rubin 1992).

The `MOSFiT` setup for the magnetar model (Kasen & Bildsten 2010; Woosley 2010) is described in detail in Nicholl et al. (2017), while the radioactive component implementation is taken from Nadyozhin (1994). The magnetar model imposes a constraint that penalizes models in which the total kinetic energy is higher than the magnetar energy plus neutrino energy, minus radiative losses. In the `slsnni` implementation we use here, we relax this constraint to allow for additional energy from the radioactive decay component, effectively allowing the total kinetic energy to be higher. The extra luminosity comes from the maximum allowed energy from burning pure helium into nickel, or $\sim 10^{52} \times (M_{\rm Ni}/M_{\odot})$ erg, where $M_{\rm Ni}$ is the total nickel mass synthesized during the explosion.

The magnetar model in `MOSFiT` has a modified blackbody spectral energy distribution, where flux blueward of a cutoff wavelength λ_0 is suppressed by a factor proportional to

[10] https://wiserep.weizmann.ac.il/

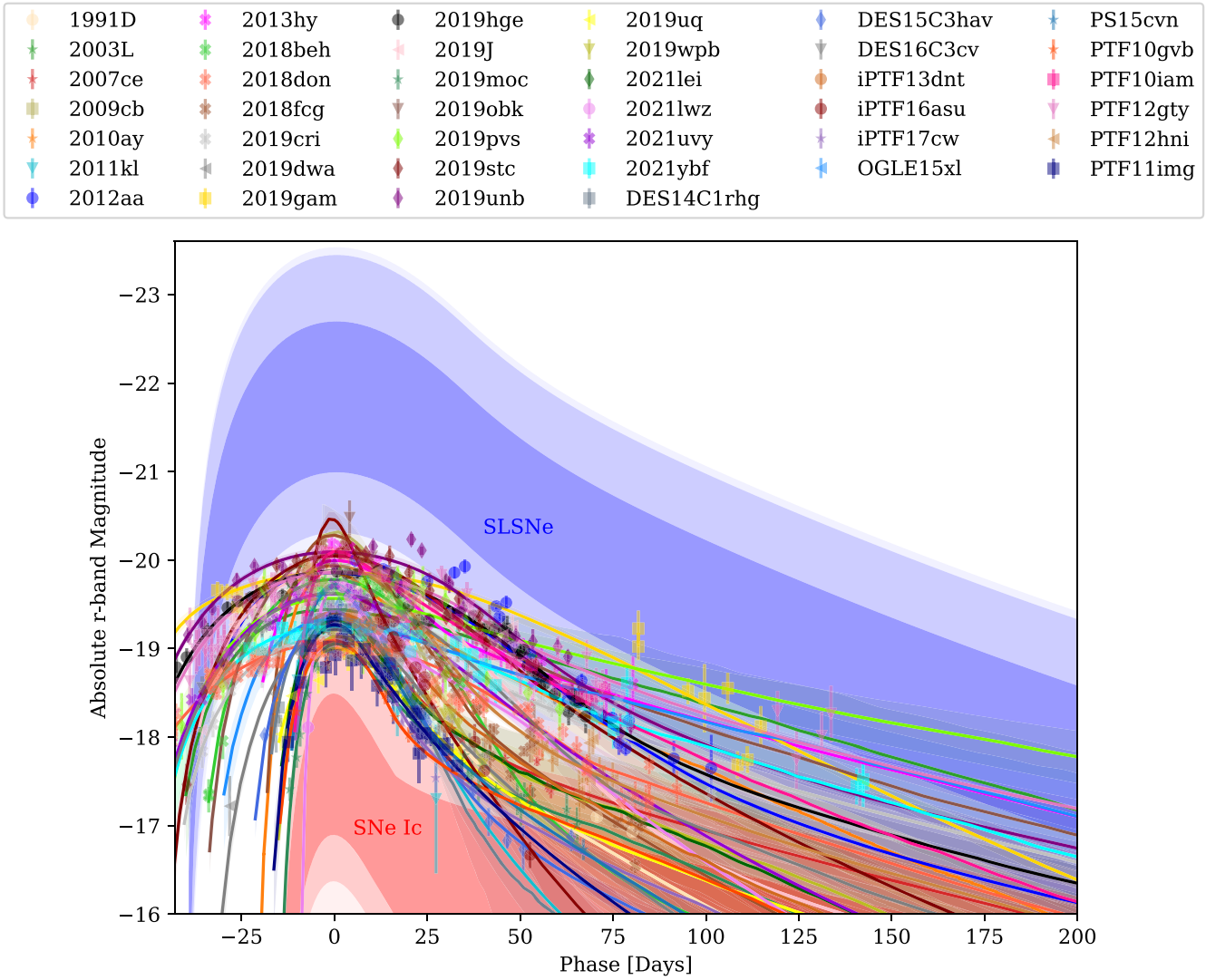

Figure 1. Light curves of all the Gold and Silver LSNe in our sample. The individual data points are *r*-band magnitudes of the SNe, and the lines are the corresponding best-fit models described in Section 3. The shaded regions represent the 1σ, 2σ, and 3σ intervals for typical light curves of SLSNe (blue) and SNe Ic (red) obtained from averaging their light-curve models.

$(\lambda/\lambda_0)^\alpha$ with a fixed $\alpha = 1$ and a variable λ_0, in order to account for the UV absorption seen in SLSNe (e.g., Yan et al. 2018). In our modified `slsnni` model we allow the power-law index α of the suppression to vary in addition to λ_0, so that we can fit all SNe with the same uniform model, regardless of the location or steepness of the suppression. We are thus also able to fit the light curves of SNe that are reddened due to line blanketing from radioactive decay.

We retain model priors similar to those Nicholl et al. (2017) used to model SLSNe, with two modifications to accommodate the wider range of SNe modeled here, encompassing the typical parameters of both SNe Ib/c and SLSNe. First, we impose a conservative upper limit on the total nickel mass fraction of $f_{\rm Ni} < 0.5$, higher than the typical ranges that SNe Ic/Ic-BL reach (Taddia et al. 2019; Barbarino et al. 2020). And second, since we are unable to constrain the value for the neutron star mass $M_{\rm NS}$ in any model, we impose a Gaussian prior of $M_{\rm NS} = 1.7 \pm 0.2\,M_\odot$, similar to previous studies (Blanchard et al. 2020), and motivated by the typical masses of neutron stars (Özel & Freire 2016). The actual choice of prior for $M_{\rm NS}$ has no effect on the output parameters since the mass of the neutron star has a negligible effect on the output light curves. In Table 2 we list all the model parameters, their priors, units, and definitions.

We fit the multiband light curves of all LSNe and list the best-fit values and uncertainties in Table 3. The uncertainties presented here represent only the statistical errors on the fits. In Table 4 we list additional parameters calculated from the posteriors of the fitted parameters. We measure the peak *r*-band magnitude of each SN from its light-curve model to quantify the peak, even for the SNe that do not have *r*-band observations available. Table 4 also lists an estimated explosion date in MJD and a rise time, defined as the time from explosion date to maximum *r*-band brightness. In the same table, we list estimates for the total kinetic energy, $E_k = (3/10) M_{\rm ej} V_{\rm ej}^2$ and total nickel mass synthesized in the explosion, $M_{\rm Ni} = f_{\rm Ni} \times M_{\rm ej}$. We include light-curve plots for all bands in Appendix H and corner plots in Appendix G for the models of all 40 LSNe in Appendix A.

We explore which areas of parameter space LSNe could exist in by generating 10,000 LSNe input light curves based on the priors listed in Table 2 and then selecting the output objects

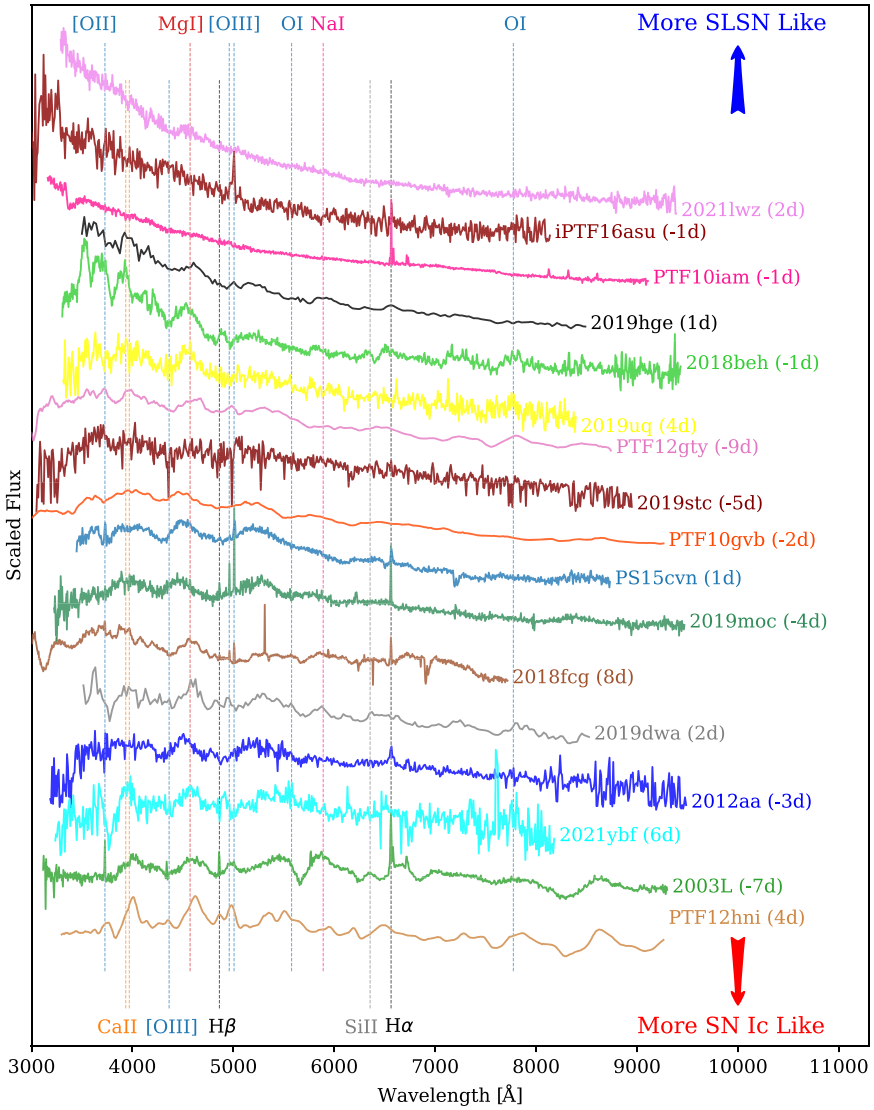

Figure 2. Representative spectra for all the Gold and Silver LSNe that have spectra available within ±10 days of peak, sorted by color and spectral features. We find that LSNe appear to form a continuous distribution, from blue SLSN-like spectra to red SN Ic-like spectra. Individual references for each spectrum are listed in Appendix A.

with a peak magnitude M_r between −19 and −20 mag. We find the input and output distributions to be similar at the ∼90% level for almost every parameter, meaning if LSNe exist within our defined prior, we would be able to recover them. The one exception is SNe that have both a $P_{\rm spin} > 9$ ms and a $f_{\rm Ni} < 0.03$, as they all fall below our lower luminosity threshold of $M_r = -19$ and would likely appear to be normal SNe Ic.

4. Modeling Results

In Figure 3 we show the distribution of the most relevant physical parameters $P_{\rm spin}$, $B_\perp$, $M_{\rm ej}$, $v_{\rm ej}$, and $f_{\rm Ni}$ for the LSNe, SLSNe, SNe Ic, and SNe Ic-BL populations. In general, we find that SLSNe and SNe Ic/Ic-BL separate well in terms of most parameters; while LSNe span the whole range of allowed parameter space. Some LSNe have magnetar parameters ($P_{\rm spin}$, $B_\perp$) that overlap the SLSNe population, consistent with powerful central engines, while some LSNe overlap the SNe Ic/Ic-BL population. The latter have weak or no evidence for magnetars, but instead appear powered by radioactive decay, as evidenced by their high $f_{\rm Ni}$ values. The ejecta masses of LSNe span a wide range, from ∼1.5 $M_\odot$ and up to ∼30 $M_\odot$. We find the ejecta velocity estimates among all types of SNe to be very similar.

4.1. Magnetar Parameters

In order to quantify how different the parameter distributions of LSNe are from those of SLSNe and SNe Ic/Ic-BL, we implement a two-sample Kolmogorov–Smirnov (K-S). A K-S metric of $D = 0.0$ indicates the two populations are drawn from the same distribution, and $D = 1.0$ means there is no overlap between the distributions. We find a K-S metric (and p-value) for the LSN distribution of $P_{\rm spin}$ of $D = 0.63$ ($<10^{-3}$) and $D = 0.62$ ($<10^{-3}$) when compared to the SLSNe and SNe Ic/Ic-BL distributions, respectively. This indicates that the spin period distribution of LSNe is not similar to that of either SLSNe or SNe Ic/Ic-BL, as LSNe span a wider range of $P_{\rm spin}$ values than either SLSNe or SNe Ic/Ic-BL. A similar result is found for the magnetic field strength, where we find values of $D = 0.34$ ($<10^{-3}$) and $D = 0.75$ ($<10^{-3}$) when LSNe are compared to SLSNe and SNe Ic/Ic-BL, respectively. This

Table 2
MOSFiT Parameter Definitions

Parameter	Prior	Units	Definition
M_{ej}	[0.1, 100]	$M_\odot$	Ejecta mass
f_{Ni}	log((0, 0.5])		Nickel mass as a fraction of the ejecta mass
v_{ej}	log([10^3, 10^5])	km s^{-1}	Ejecta velocity
M_{NS}	1.7 ± 0.2	$M_\odot$	Neutron star mass
P_{spin}	[0.7, 30]	ms	Magnetar spin
$B_\perp$	log((0, 15])	10^{14} G	Magnetar magnetic field strength
θ_{BP}	[0, $\pi/2$]	rad	Angle of the dipole moment
t_{exp}	[0, 200]	days	Explosion time relative to first data point
T_{min}	[3000, 10000]	K	Photosphere temperature floor
λ	[2000, 6000]	Å	Flux below this wavelength is suppressed
α	[0, 5]		Slope of the wavelength suppression
$n_{H,host}$	log([10^{16}, 10^{23}])	cm^{-2}	Column density in the host galaxy
κ	[0.01, 0.34]		Optical opacity
κ_γ	log([0.01, 0.5])	cm^2 g^{-1}	Gamma-ray opacity
σ	[10^{-3}, 10^2]		Uncertainty required for $\chi^2_r = 1$

Note. Parameters used in the MOSFiT model, their priors, units, and definitions. Priors noted in log have a log-flat prior, priors without it are flat in linear space, and priors with a center and error bars have a Gaussian distribution.

suggests that the LSNe $B_\perp$ distribution is very different from that of SNe Ic/Ic-BL, and still distinct (but less so) from the SLSN population.

In Figure 4 we focus on the distribution of magnetar parameters (P_{spin}, and $B_\perp$). While 90% of SLSNe have P_{spin} values $\lesssim$6.9 ms, and 90% of SNe Ic/Ic-BL have values of $P_{spin} \gtrsim 17$ ms (i.e., there is no evidence that they have a rapidly spinning magnetar engine), LSNe span the whole range of $P_{spin} \approx 2$–23 ms. Similarly, while only ~10% of SLSNe have spin periods $P_{spin} \approx 7$–17 ms (and 3% of SNe Ic/Ic-BL), 38% of LSNe lie in this intermediate range. We note that some LSNe are best fit by magnetars with very strong magnetic fields and slow spin periods. The slow spin period makes it such that the contribution from the magnetar is negligible and the magnetic field strength becomes irrelevant in terms of its effect on the output light curve for SNe with slow spin periods.

In Figure 5 we explore the relative contribution of the magnetar engine component to the total luminosity of the SNe. The left panel of Figure 5 shows how this magnetar contribution evolves as a function of time. We find that 88% of SLSNe have a significant magnetar contribution $\gtrsim$80% soon after explosion, and all SLSNe have at least some magnetar contribution above 10%. On the other hand, 60% of SNe Ic/Ic-BL have a magnetar contribution $\lesssim$10%, and only 31% have a magnetar contribution $\gtrsim$50% in the few days after explosion. LSNe span a wide range of magnetar contributions that overlap with both SLSNe and SNe Ic/Ic-BL. While 80% of LSNe have a magnetar contribution $\gtrsim$10%, 75% of them have at least a 50% magnetar contribution.

Along the same lines, in the right panel of Figure 5 we show the same fractional magnetar contribution but integrated over the first 200 days after explosion for every SN. This histogram includes 150 samples for each SN, one for each realization (or walker) of the model light curves. We mark the threshold that corresponds to $N = 1$ SN, above which we can consider the measurements to be significant. Above this threshold, 92% of SLSNe samples have a magnetar contribution >80%, and only 8% have a contribution <10%. Conversely, only 5% of SNe Ic-BL (and no SNe Ic) have a magnetar contribution >80%; and 45% and 71% of SNe Ic-BL and SNe Ic have a magnetar contribution <10%, respectively. LSNe show a more noticeable bifurcation, where 74% of samples have a magnetar contribution >80% and 27% have a magnetar contribution <10%.

4.2. Ejecta Parameters

The parameter distributions for nickel mass fraction f_{Ni} and ejecta mass M_{ej} show less stark differences between LSNe and the other populations than the magnetar parameters. We find a K-S metric (and p-value) for the distribution of f_{Ni} values of SLNe of $D = 0.23$ (0.06) and $D = 0.25$ (0.09) compared to the SLSNe and SNe Ic/Ic-BL distributions, respectively. In terms of M_{ej}, we find a metric of $D = 0.39$ ($<10^{-3}$) and $D = 0.19$ (0.34) for the same populations. With the exception of the distribution of M_{ej} between LSNe and SLSNe ($p < 10^{-3}$), we can not rule out the null hypothesis that these populations are drawn for the same distribution based on the K-S metric. Finally, we measure values of $D = 0.14$ (0.5) and $D = 0.14$ (0.74) for the distribution of v_{ej} values for LSNe compared to the SLSNe and SNe Ic/Ic-BL populations; suggesting that all populations of SNe are consistent with being drawn for the same distribution of v_{ej} values.

In Figure 6 we show the values of nickel mass as a function of ejecta mass. The main difference between SLSNe and SNe Ic is not necessarily the nickel mass or even the nickel mass fraction, but rather how well constrained this parameter is. Effectively all SNe Ic/Ic-BL have well-constrained nickel mass fractions, usually $f_{Ni} \lesssim 0.1$, which translates to a total nickel mass of $M_{Ni} \lesssim 0.5$ $M_\odot$. On the other hand, ~50% of SLSNe and LSNe have an unconstrained nickel mass fractions with an uncertainty on $\log(f_{Ni}) \gtrsim 0.5$. For some SLSNe, the posterior reaches the $f_{Ni} = 0.5$ limit imposed by the prior. In these situations, the light curves are dominated by the magnetar component, and the value for f_{Ni} can therefore not be constrained. As expected, LSNe have nickel masses that span a wide range of possibilities, while some appear magnetar dominated, others are best fit by a radioactively powered light curve. We find that the values of f_{Ni} for the radioactively dominated LSNe span the same range as SNe Ic/Ic-BL, $f_{Ni} \approx 0.01$–0.1.

Figure 7 shows how the rise time of LSNe compares to those of SLSNe and SNe Ic/Ic-BL. LSNe occupy a very distinct space in terms of peak magnitude (by definition), but also tend to have intermediate rise times between SLSNe and SNe Ic. The rise times of LSNe span the range from ~20 to ~65 days, similar but slightly shorter than the ~20 to 90 days for SLSNe, but significantly wider than the $\lesssim$30 days of SNe Ic/Ic-BL. We explore the possibility that this *broadening* of allowed rise times is caused by the underlying power source but conclude this does not appear to be the case, since we find no strong correlation between the dominant power source and the rise time of the transient. Instead, the parameter controlling the rise-time difference appears to be the ejecta mass.

The rise times of CCSNe have been shown to correlate with ejecta mass, as higher ejecta masses lead to longer rise times (e.g., Dessart et al. 2016). This correlation is to be expected

Table 3
Fitted Parameters

Name	$B_\perp$ (10^{14} G)	α	λ (1000 Å)	$f_{\rm Ni}$	κ	$\log(\kappa_\gamma)$ ($\rm cm^2\ g^{-1}$)	$M_{\rm ej}$ ($M_\odot$)	$P_{\rm spin}$ (ms)	$T_{\rm min}$ (1000 K)	$\theta_{\rm PB}$ (rad)	$V_{\rm ej}$ (1000 km $\rm s^{-1}$)
DES14C1rhg	8.5 ± 3.2	2.0 ± 1.7	2.73 ± 0.55	$0.01^{+0.03}_{-0.01}$	$0.05^{+0.05}_{-0.03}$	$0.07^{+0.19}_{-0.05}$	$4.1^{+3.7}_{-2.0}$	$10.0^{+3.1}_{-5.3}$	5.1 ± 1.54	1.06 ± 0.34	6.39 ± 0.55
DES15C3hav	$6.1^{+3.4}_{-1.6}$	0.2 ± 0.2	4.01 ± 1.31	$0.01^{+0.02}_{-0.0}$	$0.04^{+0.03}_{-0.02}$	$0.09^{+0.19}_{-0.06}$	$8.1^{+8.8}_{-3.6}$	$2.4^{+2.3}_{-1.3}$	7.56 ± 0.76	0.96 ± 0.42	6.07 ± 0.64
DES16C3cv	$0.8^{+1.0}_{-0.5}$	$3.2^{+1.0}_{-0.6}$	3.43 ± 0.19	$0.01^{+0.05}_{-0.01}$	0.28 ± 0.05	$0.01^{+0.0}_{-0.0}$	5.2 ± 1.1	4.2 ± 1.4	5.04 ± 1.44	0.29 ± 0.15	6.52 ± 0.52
iPTF13dnt	$0.1^{+2.9}_{-0.1}$	2.8 ± 1.7	4.05 ± 1.35	$0.15^{+0.11}_{-0.07}$	$0.09^{+0.08}_{-0.05}$	$0.05^{+0.21}_{-0.03}$	$9.5^{+6.8}_{-4.2}$	$20.0^{+7.0}_{-10.8}$	$3.79^{+0.83}_{-0.51}$	0.77 ± 0.56	14.08 ± 4.52
iPTF16asu	$7.9^{+3.0}_{-1.8}$	2.5 ± 0.3	5.49 ± 0.13	$0.01^{+0.02}_{-0.0}$	$0.05^{+0.06}_{-0.02}$	$0.03^{+0.04}_{-0.01}$	$0.4^{+0.6}_{-0.2}$	13.2 ± 1.5	$7.78^{+1.45}_{-3.49}$	1.02 ± 0.37	4.02 ± 0.96
iPTF17cw	11.6 ± 2.9	$2.7^{+1.2}_{-0.5}$	5.17 ± 0.31	$0.03^{+0.03}_{-0.01}$	$0.03^{+0.02}_{-0.01}$	$0.09^{+0.19}_{-0.06}$	$4.3^{+2.8}_{-1.7}$	22.5 ± 2.9	6.11 ± 0.53	1.21 ± 0.3	8.34 ± 1.24
OGLE15xl	$0.4^{+1.2}_{-0.3}$	2.2 ± 1.7	3.93 ± 1.32	$0.14^{+0.13}_{-0.07}$	$0.1^{+0.14}_{-0.06}$	0.23 ± 0.15	10.5 ± 6.5	$10.9^{+11.1}_{-6.0}$	$5.35^{+2.53}_{-1.37}$	0.8 ± 0.55	12.04 ± 4.89
PS15cvn	$0.1^{+0.5}_{-0.1}$	3.9 ± 0.7	4.79 ± 0.11	$0.03^{+0.04}_{-0.02}$	0.07 ± 0.01	$0.01^{+0.0}_{-0.0}$	$3.7^{+2.6}_{-1.6}$	19.1 ± 8.5	6.34 ± 0.22	0.64 ± 0.56	9.07 ± 0.66
PTF10gvb	$12.5^{+1.8}_{-2.9}$	$1.5^{+2.3}_{-1.1}$	$3.33^{+1.43}_{-0.89}$	$0.07^{+0.06}_{-0.02}$	$0.08^{+0.05}_{-0.03}$	$0.21^{+0.18}_{-0.11}$	4.2 ± 1.9	23.2 ± 4.2	4.85 ± 0.2	1.22 ± 0.25	14.11 ± 1.09
PTF10iam	$2.6^{+1.0}_{-0.6}$	3.4 ± 0.9	5.83 ± 0.16	< 0.01	0.02 ± 0.01	$0.1^{+0.2}_{-0.07}$	$0.9^{+1.0}_{-0.4}$	13.7 ± 1.5	6.61 ± 2.0	1.06 ± 0.37	3.02 ± 0.86
PTF11img	$0.1^{+0.8}_{-0.1}$	$1.9^{+2.0}_{-0.9}$	4.65 ± 0.67	$0.22^{+0.11}_{-0.07}$	$0.12^{+0.07}_{-0.04}$	$0.02^{+0.01}_{-0.0}$	$3.9^{+2.3}_{-1.4}$	18.5 ± 8.7	5.52 ± 0.44	0.71 ± 0.55	16.54 ± 3.12
PTF12gty	$1.6^{+1.0}_{-0.5}$	$1.3^{+2.1}_{-1.0}$	$2.95^{+1.2}_{-0.67}$	$0.02^{+0.04}_{-0.01}$	$0.16^{+0.11}_{-0.07}$	$0.15^{+0.21}_{-0.09}$	$9.6^{+7.8}_{-4.0}$	7.4 ± 0.8	5.26 ± 0.33	0.96 ± 0.41	5.79 ± 0.49
PTF12hni	$7.0^{+4.1}_{-2.4}$	$1.6^{+1.7}_{-0.9}$	$4.36^{+0.99}_{-1.76}$	$0.02^{+0.02}_{-0.01}$	$0.05^{+0.03}_{-0.02}$	$0.1^{+0.2}_{-0.08}$	14.1 ± 7.8	5.0 ± 3.2	$5.48^{+0.55}_{-0.3}$	1.08 ± 0.41	7.58 ± 1.63
SN 1991D	9.7 ± 3.2	2.1 ± 1.7	3.54 ± 1.13	$0.03^{+0.05}_{-0.02}$	0.05 ± 0.04	$0.04^{+0.05}_{-0.03}$	$5.3^{+7.4}_{-2.3}$	$3.1^{+4.8}_{-1.9}$	$4.57^{+0.38}_{-0.25}$	1.07 ± 0.34	10.45 ± 1.8
SN 2003L	$0.2^{+4.2}_{-0.2}$	2.2 ± 1.6	4.15 ± 1.35	$0.12^{+0.14}_{-0.08}$	$0.09^{+0.13}_{-0.06}$	$0.08^{+0.22}_{-0.06}$	$17.2^{+23.9}_{-9.0}$	16.6 ± 9.0	6.58 ± 2.41	0.8 ± 0.53	$9.24^{+6.22}_{-3.85}$
SN 2007ce	10.0 ± 2.7	2.6 ± 0.2	5.43 ± 0.07	0.02 ± 0.01	$0.02^{+0.01}_{-0.0}$	0.21 ± 0.15	10.1 ± 4.7	20.9 ± 5.6	7.26 ± 0.17	1.16 ± 0.31	5.84 ± 1.0
SN 2009cb	$7.2^{+4.2}_{-2.5}$	2.2 ± 1.8	2.99 ± 0.64	$0.03^{+0.04}_{-0.02}$	0.04 ± 0.02	$0.06^{+0.2}_{-0.05}$	$7.1^{+8.4}_{-3.3}$	$2.8^{+3.3}_{-1.5}$	4.74 ± 1.5	1.07 ± 0.42	9.59 ± 1.88
SN 2010ay	$0.1^{+3.2}_{-0.1}$	3.3 ± 1.1	4.7 ± 0.25	$0.15^{+0.12}_{-0.07}$	$0.02^{+0.02}_{-0.01}$	$0.03^{+0.07}_{-0.02}$	$8.1^{+6.8}_{-3.6}$	$20.7^{+6.6}_{-10.8}$	5.14 ± 1.46	0.73 ± 0.57	8.93 ± 2.31
SN 2011kl	$5.5^{+4.0}_{-2.5}$	2.1 ± 1.9	2.41 ± 0.34	0.27 ± 0.14	$0.26^{+0.05}_{-0.09}$	$0.01^{+0.0}_{-0.0}$	3.9 ± 1.8	$11.0^{+3.2}_{-2.0}$	9.35 ± 0.49	0.93 ± 0.44	22.8 ± 5.69
SN 2012aa	$4.7^{+2.2}_{-1.2}$	4.1 ± 0.7	4.84 ± 0.16	< 0.0	$0.03^{+0.03}_{-0.01}$	$0.07^{+0.22}_{-0.05}$	$26.7^{+19.0}_{-11.1}$	6.2 ± 1.9	6.45 ± 0.49	1.05 ± 0.39	2.69 ± 0.41
SN 2013hy	$5.6^{+4.3}_{-2.7}$	$2.6^{+1.5}_{-0.9}$	$3.25^{+0.27}_{-0.17}$	$0.09^{+0.11}_{-0.04}$	$0.02^{+0.02}_{-0.01}$	$0.07^{+0.19}_{-0.05}$	17.0 ± 9.6	14.0 ± 2.9	7.88 ± 0.42	0.97 ± 0.44	6.16 ± 0.71
SN 2018beh	$6.1^{+1.8}_{-1.2}$	$0.1^{+0.2}_{-0.1}$	$3.07^{+1.7}_{-0.85}$	< 0.0	$0.07^{+0.05}_{-0.03}$	$0.09^{+0.2}_{-0.06}$	$10.6^{+8.1}_{-4.1}$	$1.5^{+1.1}_{-0.5}$	4.4 ± 1.06	1.19 ± 0.32	5.79 ± 0.18
SN 2018don	0.7 ± 0.3	$4.6^{+0.3}_{-0.5}$	4.59 ± 0.06	< 0.01	0.26 ± 0.05	$0.01^{+0.0}_{-0.0}$	6.7 ± 1.4	7.8 ± 1.2	$3.91^{+0.37}_{-0.15}$	0.83 ± 0.27	5.45 ± 0.33
SN 2018fcg	$4.6^{+1.4}_{-0.9}$	$0.5^{+1.5}_{-0.3}$	3.78 ± 1.52	< 0.01	$0.09^{+0.05}_{-0.03}$	0.22 ± 0.13	2.1 ± 0.9	$6.3^{+1.6}_{-1.0}$	4.72 ± 0.13	1.13 ± 0.33	$9.17^{+0.53}_{-0.82}$
SN 2019cri	$6.5^{+4.3}_{-2.7}$	2.4 ± 1.3	5.17 ± 0.44	$0.02^{+0.02}_{-0.01}$	$0.03^{+0.03}_{-0.02}$	$0.07^{+0.21}_{-0.05}$	$25.6^{+19.9}_{-10.3}$	12.9 ± 4.0	6.05 ± 0.88	0.99 ± 0.44	3.77 ± 1.11
SN 2019dwa	$2.3^{+2.2}_{-0.9}$	$1.7^{+2.3}_{-1.4}$	$3.04^{+1.11}_{-0.74}$	$0.01^{+0.07}_{-0.01}$	0.26 ± 0.07	$0.01^{+0.01}_{-0.0}$	2.7 ± 0.9	12.5 ± 2.0	4.67 ± 0.4	0.94 ± 0.42	8.59 ± 0.79
SN 2019gam	$5.0^{+3.7}_{-2.1}$	2.4 ± 1.7	$4.46^{+0.68}_{-0.3}$	0.07 ± 0.04	$0.28^{+0.05}_{-0.08}$	$0.02^{+0.02}_{-0.01}$	29.5 ± 8.4	$3.1^{+3.5}_{-2.0}$	$9.28^{+0.53}_{-1.13}$	1.09 ± 0.36	14.23 ± 3.68
SN 2019hge	$2.3^{+1.0}_{-0.5}$	$0.2^{+0.2}_{-0.1}$	3.69 ± 1.28	$0.01^{+0.01}_{-0.0}$	$0.05^{+0.04}_{-0.02}$	$0.06^{+0.21}_{-0.04}$	$16.7^{+16.0}_{-6.8}$	$1.7^{+1.4}_{-0.7}$	5.42 ± 1.71	1.04 ± 0.39	3.61 ± 0.32
SN 2019J	$5.2^{+2.3}_{-1.2}$	$1.1^{+1.9}_{-0.8}$	$2.63^{+1.31}_{-0.48}$	< 0.0	$0.06^{+0.06}_{-0.03}$	$0.06^{+0.19}_{-0.05}$	$13.7^{+11.7}_{-5.7}$	$1.2^{+0.7}_{-0.4}$	$9.29^{+0.5}_{-0.79}$	1.01 ± 0.4	4.06 ± 0.95
SN 2019moc	$0.1^{+0.4}_{-0.0}$	4.2 ± 0.7	4.61 ± 0.13	$0.1^{+0.06}_{-0.04}$	0.02 ± 0.01	$0.05^{+0.18}_{-0.04}$	$4.4^{+3.0}_{-1.8}$	19.9 ± 8.0	$4.26^{+0.58}_{-0.28}$	0.63 ± 0.54	8.08 ± 1.11
SN 2019obk	$3.4^{+2.7}_{-1.3}$	$0.8^{+2.1}_{-0.7}$	$3.28^{+1.46}_{-0.92}$	$0.03^{+0.04}_{-0.01}$	$0.03^{+0.04}_{-0.02}$	$0.09^{+0.19}_{-0.06}$	$14.5^{+20.3}_{-7.9}$	8.8 ± 1.5	$6.49^{+1.32}_{-0.71}$	0.92 ± 0.46	6.92 ± 1.23
SN 2019pvs	$1.5^{+3.7}_{-0.8}$	$1.8^{+2.1}_{-1.4}$	3.2 ± 0.94	$0.03^{+0.07}_{-0.02}$	$0.03^{+0.05}_{-0.02}$	$0.16^{+0.2}_{-0.11}$	$16.2^{+16.7}_{-9.0}$	$9.1^{+3.3}_{-1.5}$	8.71 ± 1.03	0.8 ± 0.53	$4.48^{+2.17}_{-1.04}$
SN 2019stc	$1.5^{+1.2}_{-0.6}$	$1.1^{+1.9}_{-0.7}$	$4.34^{+0.89}_{-1.64}$	$0.02^{+0.1}_{-0.01}$	0.24 ± 0.07	$0.01^{+0.01}_{-0.0}$	$4.0^{+2.1}_{-1.1}$	7.7 ± 1.0	$5.51^{+0.52}_{-0.96}$	0.92 ± 0.44	6.71 ± 1.09
SN 2019unb	$2.2^{+1.8}_{-0.7}$	$0.2^{+0.4}_{-0.1}$	3.58 ± 1.51	$0.01^{+0.03}_{-0.01}$	$0.06^{+0.06}_{-0.03}$	$0.1^{+0.19}_{-0.07}$	$15.2^{+12.0}_{-6.5}$	1.9 ± 0.8	8.41 ± 1.33	0.98 ± 0.47	4.22 ± 0.5
SN 2019uq	10.2 ± 3.5	2.0 ± 1.8	3.07 ± 0.85	$0.02^{+0.03}_{-0.01}$	$0.03^{+0.03}_{-0.01}$	$0.05^{+0.21}_{-0.04}$	$7.9^{+6.6}_{-3.8}$	17.0 ± 5.3	$5.86^{+1.13}_{-1.83}$	1.11 ± 0.36	6.99 ± 1.26
SN 2019wpb	$0.1^{+0.5}_{-0.1}$	3.0 ± 1.5	$4.3^{+0.52}_{-0.93}$	$0.08^{+0.06}_{-0.03}$	$0.02^{+0.02}_{-0.01}$	$0.07^{+0.22}_{-0.05}$	$7.4^{+5.0}_{-3.2}$	$21.5^{+6.5}_{-9.9}$	4.08 ± 0.81	0.74 ± 0.57	9.88 ± 2.0

Table 3
(Continued)

Name	$B_\perp$ (10^{14} G)	α	λ (1000 Å)	$f_{\rm Ni}$	κ	$\log(\kappa_\gamma)$ ($\rm cm^2\ g^{-1}$)	$M_{\rm ej}$ ($M_\odot$)	$P_{\rm spin}$ (ms)	$T_{\rm min}$ (1000 K)	$\theta_{\rm PB}$ (rad)	$V_{\rm ej}$ (1000 km $\rm s^{-1}$)
SN 2021lei	$0.1^{+1.0}_{-0.1}$	2.7 ± 1.4	4.79 ± 0.47	0.1 ± 0.05	$0.04^{+0.04}_{-0.02}$	$0.08^{+0.19}_{-0.06}$	$7.8^{+4.6}_{-2.8}$	20.1 ± 8.4	4.31 ± 1.0	0.73 ± 0.58	12.8 ± 4.19
SN 2021lwz	$4.0^{+1.7}_{-0.8}$	3.8 ± 1.0	3.59 ± 0.36	$0.01^{+0.02}_{-0.0}$	$0.03^{+0.02}_{-0.01}$	$0.1^{+0.2}_{-0.08}$	$0.4^{+0.6}_{-0.2}$	11.0 ± 2.0	6.55 ± 2.45	1.04 ± 0.37	2.98 ± 0.31
SN 2021uvy	$1.5^{+1.3}_{-0.5}$	$0.2^{+0.6}_{-0.2}$	$2.89^{+1.67}_{-0.71}$	$0.01^{+0.06}_{-0.0}$	0.25 ± 0.07	$0.01^{+0.0}_{-0.0}$	3.8 ± 1.0	5.9 ± 1.0	$9.64^{+0.27}_{-0.78}$	0.91 ± 0.48	5.5 ± 0.46
SN 2021ybf	$0.2^{+2.3}_{-0.2}$	$1.8^{+2.1}_{-1.4}$	3.44 ± 1.01	$0.08^{+0.08}_{-0.04}$	$0.05^{+0.05}_{-0.03}$	$0.07^{+0.2}_{-0.05}$	$20.1^{+16.9}_{-10.4}$	18.5 ± 8.2	4.39 ± 1.02	0.74 ± 0.54	6.15 ± 1.01

Note. Full list of the best-fit parameters from the `MOSFiT` model to all the LSNe in our sample. The definitions and priors of all parameters are given in Table 2. Additional parameters derived from these posteriors are listed in Table 4. The only parameter excluded from this table is the mass of the neutron star $M_{\rm NS}$, since it is effectively equal to the prior for all objects.

(This table is available in machine-readable form.)

Table 4
Additional Parameters

Name	Absolute r-mag	Explosion Date (MJD)	Rise Time (days)	$A_{V,\mathrm{host}}$ (mag)	E_k (10^{51} erg)	M_{Ni} ($M_\odot$)	WAIC
DES14C1rhg	$-19.40^{+0.03}_{-0.02}$	56983.2 ± 2.2	21.0 ± 1.6	<0.05	$1.3^{+1.4}_{-0.6}$	$0.04^{+0.15}_{-0.03}$	51
DES15C3hav	-19.35 ± 0.04	57303.1 ± 1.0	24.6 ± 1.0	0.71 ± 0.23	$1.7^{+1.9}_{-0.8}$	$0.08^{+0.13}_{-0.06}$	64
DES16C3cv	-19.62 ± 0.03	57578.1 ± 2.9	57.2 ± 1.9	<0.11	1.3 ± 0.4	$0.06^{+0.27}_{-0.05}$	105
iPTF13dnt	$-19.40^{+0.07}_{-0.28}$	$56529.3^{+9.9}_{-27.2}$	26.0 ± 19.3	<0.06	$11.8^{+16.7}_{-7.4}$	$1.28^{+1.09}_{-0.43}$	16
iPTF16asu	-20.46 ± 0.10	57513.4 ± 1.1	10.1 ± 1.2	<0.02	$0.04^{+0.09}_{-0.02}$	$0.003^{+0.007}_{-0.002}$	135
iPTF17cw	$-19.40^{+0.03}_{-0.02}$	57754.1 ± 0.7	13.9 ± 1.1	<0.02	$1.8^{+1.5}_{-0.8}$	$0.14^{+0.06}_{-0.09}$	32
OGLE15xl	-19.36 ± 0.25	57320.8 ± 2.9	36.3 ± 5.2	<0.21	$8.7^{+17.4}_{-6.1}$	$1.65^{+0.55}_{-0.88}$	34
PS15cvn	-19.64 ± 0.04	57326.6 ± 0.4	15.8 ± 0.3	<0.01	$0.8^{+0.2}_{-0.1}$	0.14 ± 0.09	116
PTF10gvb	-19.10 ± 0.04	55314.7 ± 0.9	17.9 ± 0.9	<0.04	5.0 ± 2.4	0.31 ± 0.06	70
PTF10iam	-20.10 ± 0.03	$55338.3^{+1.0}_{-1.7}$	13.7 ± 1.8	<0.04	$0.05^{+0.12}_{-0.03}$	$0.005^{+0.011}_{-0.003}$	56
PTF11img	-19.27 ± 0.03	55743.9 ± 1.2	19.0 ± 1.1	<0.04	$6.5^{+6.9}_{-3.4}$	$0.84^{+0.2}_{-0.11}$	52
PTF12gty	-19.86 ± 0.03	56071.0 ± 2.1	61.3 ± 2.2	<0.09	$1.9^{+1.9}_{-0.8}$	$0.18^{+0.46}_{-0.15}$	92
PTF12hni	-19.94 ± 0.04	56126.1 ± 5.3	26.3 ± 5.4	<0.08	$4.8^{+4.1}_{-2.7}$	$0.35^{+0.09}_{-0.16}$	71
SN 1991D	$-20.10^{+0.34}_{-0.58}$	48263.7 ± 6.8	15.3 ± 9.0	<0.06	$3.6^{+4.5}_{-1.8}$	0.2 ± 0.11	21
SN 2003L	-19.50 ± 0.20	$52635.9^{+3.2}_{-9.9}$	47.4 ± 15.2	<0.33	$10.4^{+21.5}_{-8.3}$	$1.97^{+1.64}_{-0.63}$	-3
SN 2007ce	-19.33 ± 0.10	54200.1 ± 5.2	18.2 ± 5.8	<0.02	2.0 ± 1.0	0.21 ± 0.05	140
SN 2009cb	-20.33 ± 0.32	$54881.7^{+6.3}_{-10.0}$	16.4 ± 8.8	$0.04^{+0.62}_{-0.04}$	$4.3^{+4.5}_{-2.4}$	$0.21^{+0.28}_{-0.18}$	33
SN 2010ay	-19.87 ± 0.08	55249.8 ± 0.5	21.2 ± 1.7	<0.05	$3.7^{+6.5}_{-2.2}$	1.19 ± 0.13	14
SN 2011kl	-19.73 ± 0.10	55903.8 ± 2.9	16.0 ± 1.8	<0.06	$12.1^{+17.3}_{-7.2}$	$1.06^{+1.05}_{-0.68}$	11
SN 2012aa	-19.86 ± 0.06	55921.0 ± 3.1	37.9 ± 3.9	<0.04	$1.1^{+1.0}_{-0.4}$	$0.09^{+0.1}_{-0.05}$	65
SN 2013hy	-20.00 ± 0.04	56515.9 ± 2.2	26.8 ± 1.6	<0.03	3.8 ± 2.5	$1.76^{+0.25}_{-0.51}$	109
SN 2018beh	-19.78 ± 0.01	58212.9 ± 0.4	37.8 ± 0.4	<0.03	$2.1^{+1.7}_{-0.9}$	$0.03^{+0.03}_{-0.01}$	211
SN 2018don	-19.06 ± 0.01	58198.6 ± 1.0	74.1 ± 1.0	$0.01^{+0.33}_{-0.01}$	1.2 ± 0.3	$0.02^{+0.06}_{-0.01}$	967
SN 2018fcg	-20.28 ± 0.03	58336.8 ± 0.8	20.3 ± 0.7	<0.02	$1.0^{+0.6}_{-0.3}$	$0.01^{+0.02}_{-0.0}$	235
SN 2019cri	$-19.10^{+0.08}_{-0.05}$	58560.4 ± 2.5	47.0 ± 2.9	<0.08	$2.1^{+2.8}_{-1.2}$	0.52 ± 0.23	54
SN 2019dwa	-19.21 ± 0.03	58576.2 ± 1.1	34.7 ± 1.5	<0.03	1.2 ± 0.5	$0.04^{+0.21}_{-0.04}$	79
SN 2019gam	$-19.90^{+0.13}_{-0.08}$	$58607.1^{+4.1}_{-7.7}$	55.6 ± 6.7	<0.09	36.3 ± 21.3	2.15 ± 1.3	52
SN 2019hge	-19.87 ± 0.02	58625.6 ± 1.1	58.9 ± 1.1	0.51 ± 0.19	$1.3^{+1.2}_{-0.5}$	$0.1^{+0.2}_{-0.07}$	145
SN 2019J	-19.87 ± 0.11	58487.1 ± 3.0	41.5 ± 3.0	<0.08	$1.3^{+1.4}_{-0.5}$	$0.03^{+0.04}_{-0.02}$	28
SN 2019moc	-19.06 ± 0.04	$58691.9^{+0.1}_{-0.2}$	15.4 ± 0.6	<0.02	$1.7^{+1.6}_{-0.8}$	0.43 ± 0.03	81
SN 2019obk	-20.06 ± 0.05	58689.1 ± 1.0	37.3 ± 0.9	<0.04	$4.2^{+6.6}_{-2.5}$	0.55 ± 0.51	45
SN 2019pvs	-19.58 ± 0.10	$58678.6^{+4.7}_{-7.7}$	53.8 ± 7.6	<0.05	$1.9^{+5.5}_{-1.2}$	$0.58^{+1.33}_{-0.55}$	10
SN 2019stc	-20.05 ± 0.04	58735.6 ± 1.5	48.6 ± 1.4	<0.04	$1.0^{+0.9}_{-0.4}$	$0.08^{+0.44}_{-0.07}$	64
SN 2019unb	-20.09 ± 0.05	58763.7 ± 1.7	59.9 ± 2.5	0.53 ± 0.26	$1.5^{+1.5}_{-0.6}$	$0.17^{+0.47}_{-0.14}$	63
SN 2019uq	-19.00 ± 0.06	58482.8 ± 2.0	22.2 ± 2.2	<0.05	$2.3^{+2.3}_{-1.3}$	0.23 ± 0.15	31
SN 2019wpb	-19.14 ± 0.06	58808.9 ± 0.9	18.5 ± 1.6	<0.02	$4.1^{+4.5}_{-2.3}$	0.63 ± 0.08	43
SN 2021lei	-19.33 ± 0.04	59326.3 ± 1.2	19.1 ± 1.4	<0.05	8.6 ± 7.0	0.74 ± 0.16	50
SN 2021lwz	$-19.70^{+0.02}_{-0.01}$	59341.4 ± 0.1	9.7 ± 0.1	0.50 ± 0.07	$0.02^{+0.04}_{-0.01}$	$0.002^{+0.007}_{-0.002}$	336
SN 2021uvy	-19.62 ± 0.03	59391.6 ± 1.7	56.5 ± 2.9	0.62 ± 0.17	0.7 ± 0.3	$0.02^{+0.26}_{-0.02}$	67
SN 2021ybf	-19.26 ± 0.04	59419.1 ± 4.7	54.1 ± 4.9	<0.05	$4.4^{+4.7}_{-2.5}$	$1.74^{+0.22}_{-0.33}$	81

Note. Parameters derived from the `MOSFiT` light-curve models: the peak absolute magnitude in the observer r band (after correcting for extinction and cosmological K-correction of $+2.5 \times \log(1+z)$), the average rest-frame days from explosion to peak in the r band, the intrinsic host extinction in the V band, the kinetic energy, the total nickel mass, and the Watanabe–Akaike information criterion (WAIC) for fit quality (Watanabe 2010; Gelman et al. 2014).

(This table is available in machine-readable form.)

since the diffusion timescale is proportional to $\propto(M_{\mathrm{ej}}/v_{\mathrm{ej}})^{1/2}$, and shown to be evident in SLSNe (e.g., Nicholl et al. 2015; Könyves-Tóth & Vinkó 2021). In Figure 8 we show this trend for all SNe in our sample and see that it appears to also apply to LSNe. None of the fast-evolving LSNe with rise times <25 days have high ejecta masses above 20 $M_\odot$, and most of the slowly evolving LSNe with rise times >30 days have ejecta masses between 10 and 40 $M_\odot$. Out of the 40 LSNe, four (SN 2019dwa, SN 2019stc, SN 2021uvy, and DES16C3cv) appear to deviate from this trend, since they have rise times between 30 and 70 days but ejecta masses $<6\,M_\odot$.

Khatami & Kasen (2019) proposed a model that relates the rise time of an SN to its peak luminosity, and found that radioactively powered SNe might have nickel masses that are overestimated when using an Arnett model compared to numerical radiation transport calculations. The authors propose to use an additional dimensionless β parameter to correct for this discrepancy. The effects of this modification to the Arnett model would be most noticeable in the SNe with the longest rise times, but only affect radioactively dominated SNe. Therefore, we find that the relatively rapidly rising SNe Ib/c population and the magnetar-dominated SLSNe population are mostly unaffected. LSNe on the other hand, are the most

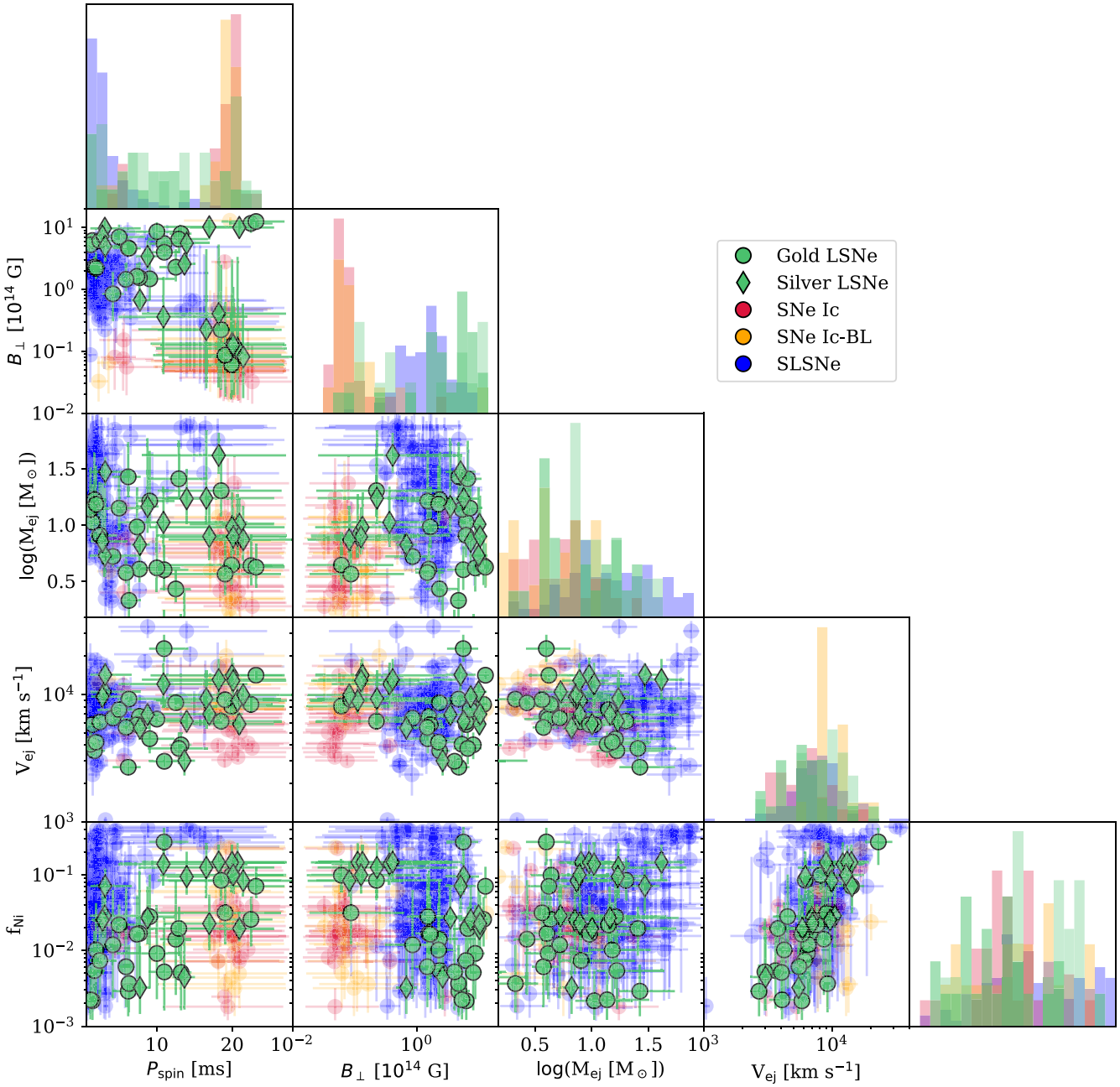

Figure 3. Best-fit MOSFiT parameters for the SLSNe, SNe Ic, SNe Ic-BL, and LSNe populations. The green circles represent the Gold LSNe sample, while the diamonds represent the Silver sample. Other SNe types are shown as faded circles for comparison. We see that SLSNe and SNe Ic/Ic-BL separate very well in terms of most parameters, while LSNe span almost the entire range of allowable models, further emphasizing their intermediate nature.

affected. We explore the effects this assumption would have on our measurements of f_{Ni} by using the comparison between an Arnett model and the Khatami model from Afsariardchi et al. (2021), who provide a relation between the Arnett and the Khatami models for a range of CCSNe. We find that the majority of SNe presented here have values of M_{Ni} that are consistent with the uncertainties produced by assuming the Khatami model versus an Arnett model, within the 1σ error bars. Some exceptions are a few Ic-like LSNe with large values of f_{Ni}: iPTF17cw, OGLE15xl, PTF11img, SN 2010a, SN 2019wpb, SN 2021lei, and SN 2021ybf. If we were to implement the Khatami model assumption onto the MOSFiT models, we might expect the f_{Ni} values of these SNe to be reduced by around half.

In Figure 9 we show the pre-explosion mass distribution for the LSNe, SLSNe, SNe Ic, and SNe Ic-BL populations, calculated by summing the posteriors for the ejecta mass and neutron star mass of each SN. The histogram includes 150 samples for each SN, one for each model realization (or walker). We indicate with a shaded region the threshold where the number of samples is equivalent to one SN, below which the measurements are not significant. The distribution of LSNe pre-explosion masses is intermediate to those of SLSNe and SNe Ic/Ic-BL. This is particularly evident at the high-mass end, where the populations appear clearly distinct. LSNe extend to masses of $\sim$30 $M_\odot$, higher than the $\sim$20 $M_\odot$ limit for SNe Ic/Ic-BL, but not as high as SLSNe, which extend up to $\sim$40 $M_\odot$. While SLSNe have a sharp drop-off at the low-mass

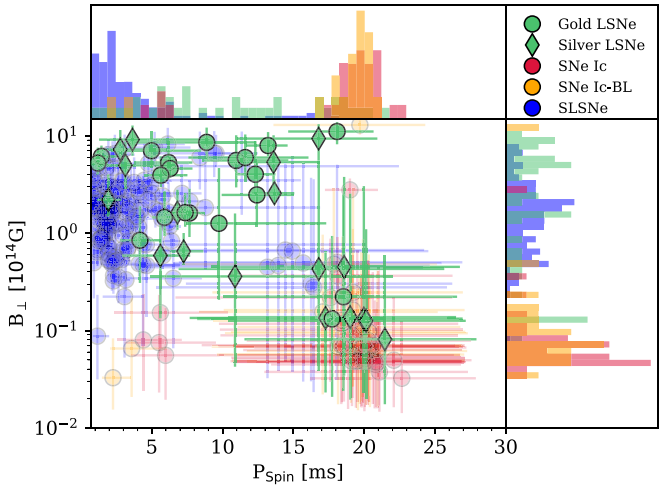

Figure 4. Best-fit magnetar spin period and magnetic field values for the LSNe, SLSNe, SNe Ic, and SNe Ic-BL populations. The upper left corner, where most SLSNe lie, is dominated by powerful fast-spinning magnetars, whereas in the bottom right corner, populated by SNe Ic/Ic-BL, the magnetar power is low and the observed optical emission is dominated by radioactive decay. Some LSNe appear powered by magnetars similar to those in SLSNe, some have intermediate power magnetars, and some have weak or no magnetar contribution.

end below $\sim 2\ M_\odot$, the mass distribution for LSNe extends as low as those of SNe Ic/Ic-BL, down to $\sim 1.5\ M_\odot$. To quantify this distinction we fit a linear slope of the form $dN/d\log M \propto M^\alpha$ to the mass distribution above 10 $M_\odot$ and up to where the distributions reach the 1 SN threshold and find best-fit values of α for the different populations of: $\alpha = -1.26 \pm 0.04$ (SLSNe), $\alpha = -1.83 \pm 0.07$ (LSNe), $\alpha = -3.21 \pm 0.23$ (SN Ic), $\alpha = -3.02 \pm 0.26$ (SN Ic-BL). LSNe have a steeper slope than SLSNe, but shallower than SNe Ic/Ic-BL, suggesting their progenitors might be a mix of SLSN-like and SNe Ic-like. The value we obtain for SLSNe perfectly matches the one found by Blanchard et al. (2020) of $\alpha = -1.26 \pm 0.06$. We find the peaks of the distributions to be $\sim 3.5\ M_\odot$ (SNe Ic-BL), $\sim 4.0\ M_\odot$ (SNe Ic), $\sim 5.6\ M_\odot$ (LSNe), and $\sim 6.6\ M_\odot$ (SLSNe). Our estimate for the peak of the SLSNe distribution is higher than the $\sim 4\ M_\odot$ found by Blanchard et al. (2020) as a result of our models allowing for an additional energy component from radioactive decay that is not present in their models.

4.3. Comparison to Other Studies

We compare our best-fit M_{ej} values obtained from MOSFiT to the results from several independent studies. Taddia et al. (2019) and Barbarino et al. (2020) fit the bolometric light curves of SNe Ic-BL and SNe Ic, respectively, with an Arnett model (Arnett 1982) to measure the ejecta masses of these SNe. Könyves-Tóth & Vinkó (2021) used a combination of bolometric light-curve models and ejecta velocity measurements to estimate the ejecta mass of SLSNe. Jerkstrand et al. (2017) modeled the spectra of SLSNe with the SUMO spectral synthesis code (Jerkstrand et al. 2012) to select the best ejecta mass estimates from a grid of models. And finally, Mazzali et al. (2016) modeled the spectra of SLSNe using a Monte Carlo spectral synthesis code (Mazzali & Lucy 1993) to infer the ejecta masses of SLSNe.

We find our estimates of M_{ej} for SLSNe and SNe Ic/Ic-BL to be in good agreement with values estimated by these studies. Five of the LSNe in this work are included in these studies. We find an ejecta mass for SN 2011kl of $M_{ej} = 3.9 \pm 1.8\ M_\odot$, consistent with the estimate of $M_{ej} = 2$–$3\ M_\odot$ from Mazzali et al. (2016). We estimate $M_{ej} = 9.6^{+7.8}_{-4.0}\ M_\odot$ for PTF12gty, within 2σ of the average ejecta mass estimate of $M_{ej} = 20.7 \pm 6.0\ M_\odot$ found by Könyves-Tóth & Vinkó (2021), but consistent with their Equation (8) estimate of $M_{ej} = 14.68\ M_\odot$. The ejecta masses we find for iPTF13dnt ($9.5^{+6.8}_{-4.2}\ M_\odot$), iPTF16asu ($0.4^{+0.6}_{-0.2}\ M_\odot$), and iPTF17cw ($4.3^{+2.8}_{-1.7}\ M_\odot$) are all within 1σ of the estimates from Taddia et al. (2019) of $7.0 \pm 2.6\ M_\odot$, $0.9 \pm 0.1\ M_\odot$, and $4.5 \pm 1.8\ M_\odot$, respectively. Benetti et al. (2002) estimate the ejecta mass of SN 1991D to be 1.2–2.5 $M_\odot$ from semi-analytical light-curve models, or 1.2σ lower than our estimate of $M_{ej} = 5.3^{+7.4}_{-2.3}\ M_\odot$. Roy et al. (2016) find an ejecta mass for SN 2012aa of $M_{ej} \sim 14\ M_\odot$ and a maximum of $M_{ej} \sim 24\ M_\odot$, consistent with our estimate of $M_{ej} = 26.7^{+19.0}_{-11.1}\ M_\odot$.

4.4. Summary

We determined that LSNe have ejecta masses in between those of SLSNe and SNe Ic/Ic-BL, and magnetar parameters (P_{spin}, $B_\perp$) that span the entire range of allowed parameter space, emphasizing their intermediate nature and the contribution to their luminosity from both magnetar engines and radioactive decay. While SLSNe appear to have fast spins and strong magnetic fields, SNe Ic/Ic-BL have weak or no magnetars. This agrees with the idea that SLSNe are powered by a magnetar central engine, whereas there is no evidence for a significant magnetar contribution in SNe Ic/Ic-BL. In terms of their pre-explosion masses, LSNe extend to higher masses than SNe Ic/Ic-BL, but not as massive as SLSNe, and while SLSNe have a sharp drop-off at the low-mass end, the ejecta masses of LSNe extend as low as those of SNe Ic/Ic-BL. We find that LSNe tend to be powered either by an overabundant production of ^{56}Ni or by weak magnetar engines.

5. LSN Subgroups

LSNe span a wide range of both observational properties and model parameters. Significant differences within the LSNe population exist and they are unlikely to all be a product of the same physical process. In this section, we attempt to group LSNe into distinct subgroups with uniform spectral and photometric properties based on the labels designated in Table 1. We label each LSN with either a "Superluminous" label if their spectra are SLSN-like or "Normal" if their spectra are Ic-like. Similarly, we use a "Fast" label if their rise times are $\lesssim$25 days like most SNe Ic or "Slow" if they are $\gtrsim$35 days like most SLSNe. Given their intermediate nature, we resort to labeling some LSNe as having "Ambiguous" spectra consistent with either an SLSN or an SN Ib/c, or a light curve with "Medium" rise time between 25 and 35 days. This breakdown leads to four main groups: Slow SLSN-like, Fast SLSN-like, Slow Ic-like, and Fast Ic-like. We include an "Other" group for the LSNe that do not clearly fit into any of the previous four groups. Of the 40 Gold and Silver LSNe presented here, Slow SLSN-like make up 23% ($N = 9$), Fast SLSN-like 18% ($N = 7$), Slow Ic-like 15% ($N = 6$), Fast Ic-like 30% ($N = 12$), and 15% ($N = 6$) are in the Other group.

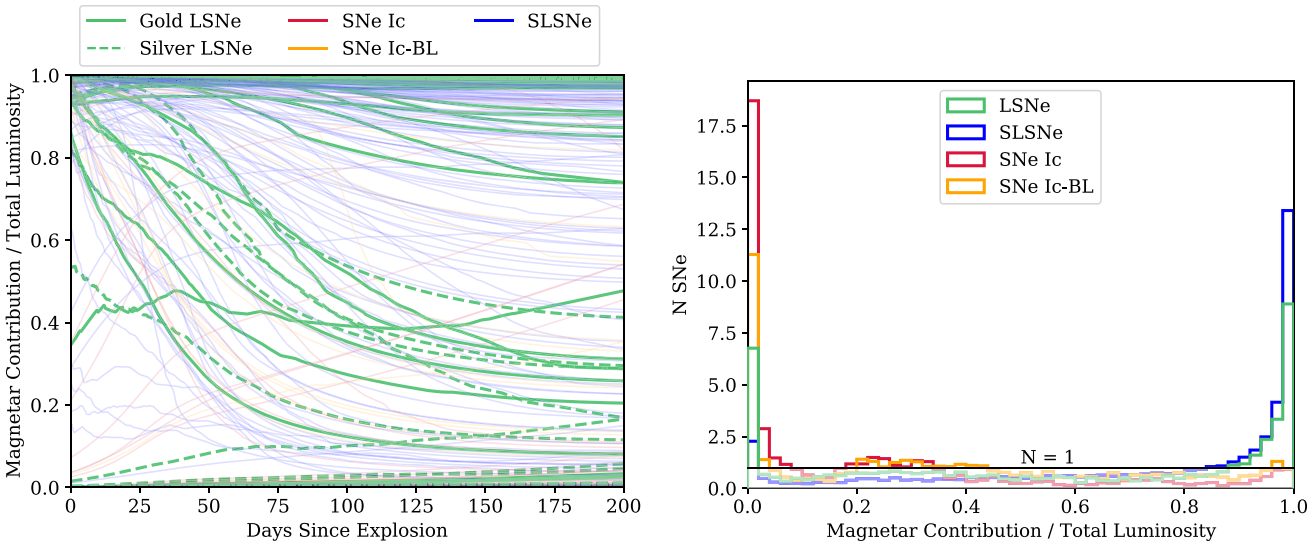

Figure 5. Left: fractional contribution of the magnetar component to the total output luminosity of the light curve (magnetar plus radioactive decay) for all the SNe in our sample as a function of days since explosion. Right: posterior model distribution for the same fractional magnetar contribution, but integrated over the first 200 days of the SN. We include 150 samples for each SN and normalize the populations by their respective sample sizes. SLSNe appear magnetar dominated and mostly remain as such throughout their evolution, whereas SNe Ic are mostly radioactively dominated. While some LSNe appear magnetar dominated, some seem to be powered entirely by radioactive decay.

5.1. Slow SLSN-like

This is the group most similar to normal SLSNe (Figure 10). The objects we group here are: SN 2013hy, SN 2018beh, SN 2019gam, SN 2019hge, and SN 2019J, SN 2019obk, SN 2019pvs, SN 2019unb, and PTF12gty. These LSNe have spectra that closely resemble those of SLSNe, and broad light curves reminiscent of SLSNe. Nevertheless, they are dimmer than typical SLSNe. This group of LSNe has the most energetic magnetars of the LSNe population, with typical spin periods $\lesssim$10 ms and magnetar magnetic fields $\gtrsim 10^{14}$ G. Their magnetic fields are similar to those of normal SLSNe, which span the $\sim$0.4–60 $\times 10^{14}$ G range, but their spin periods extend to higher values than the $P_{\rm spin} \lesssim 6$ ms found in most SLSNe, and is likely the reason for their lower luminosity. The fact that some of these LSNe have magnetars with stronger magnetic fields than some normal SLSNe suggests magnetic field strength might not be the dominant parameter powering SLSNe, particularly for slow spin periods. Compared to the rest of the LSN population, this group has the largest ejecta masses, all $\gtrsim 10\ M_{\odot}$. The power behind their light curves is also greatly dominated by the magnetar component, where all but two SNe have a magnetar contribution >90%; SN 2013hy and SN 2019pvs are the exception with a magnetar contribution of $\sim$50%.

Almost all LSNe in this group have relatively low ejecta velocities $V_{\rm ej} \lesssim 6000$ km s^{-1}, which is likely contributing to their low peak luminosity, as low ejecta velocities increase the diffusion time, distributing the output luminosity over a larger stretch of time. Two exceptions are SN 2019gam and SN 2019obk, which have ejecta velocities of $\approx$14,000 km s^{-1} and $\approx$8200 km s^{-1}, respectively. It is possible these two objects are just normal SLSNe but are marginally under-luminous due to either the slow spin period of $\approx$9 ms for SN 2019obk, or low magnetic field of $\approx 0.7 \times 10^{14}$ G for SN 2019gam.

This group of LSNe appears to be powered by magnetar engines, have light-curve durations similar to those of SLSNe, and has spectra consistent with SLSNe. Therefore, these LSNe can be considered to be the faintest SLSNe known, extending down to $M_r \sim -19.5$ mag, and likely under-luminous due to their slower spin periods than typical SLSNe.

5.2. Fast SLSN-like

We find seven LSNe that appear spectroscopically consistent with being SLSNe, but have light curves that are much faster than normal SLSNe (Figure 11). These objects are iPTF16asu, PTF10iam, DES14C1rhg, DES15C3hav, SN 2011kl, SN 2021lwz, and SN 2009cb. Even though the decline time of PTF10iam is relatively long, we include it in this group given that it has a rise time of $\sim$14 days, among the fastest of all LSNe. All objects in this group have very strong magnetic fields $\gtrsim 4 \times 10^{14}$ G (higher than normal SLSNe), but slow spin periods $\gtrsim$5 ms, leading to their low luminosities and fast timescales.

The light curves of Fast SLSN-like LSNe also appear largely dominated by a magnetar engine, where all have magnetar contributions >90%, except for SN 2011kl, which has a $\sim$75% magnetar contribution. Almost all the SNe in this group have low ejecta masses $M_{\rm ej} \lesssim 4\ M_{\odot}$ (except for SN 2009cb with $M_{\rm ej} \approx 7\ M_{\odot}$), which lies in stark contrast to the LSNe in the Slow SLSN-like group, which have ejecta masses $\gtrsim 10\ M_{\odot}$. This is to be expected, since higher ejecta masses correlate to longer diffusion times, as discussed in Section 4.2.

LSNe in this group appear to be an extension of the SLSN population, given their spectra and physical parameters, but they have relatively fast-evolving light curves due to their low ejecta masses.

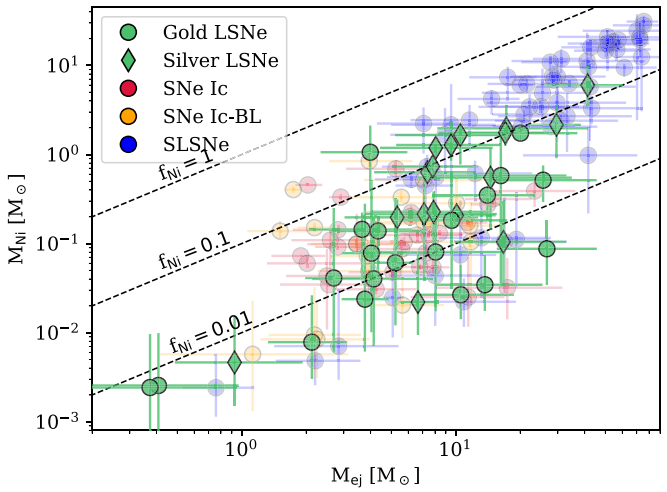

Figure 6. Best-fit nickel mass as a function of ejecta mass for the LSNe, SLSNe, SNe Ic, and SNe Ic-BL populations. For clarity, we exclude the SLSNe with unconstrained nickel mass fractions (i.e., those for which even $f_{Ni} = 0.5$ still provides a subdominant contribution to the light curve). The dashed lines indicate $f_{Ni} = 0.01$, 0.1, 1. LSNe mostly occupy a similar range to SNe Ic/Ic-BL, but also overlap the parameter space occupied by SLSNe. The higher luminosities of LSNe compared to SNe Ic/Ic-BL indicates an additional contribution from magnetar engines.

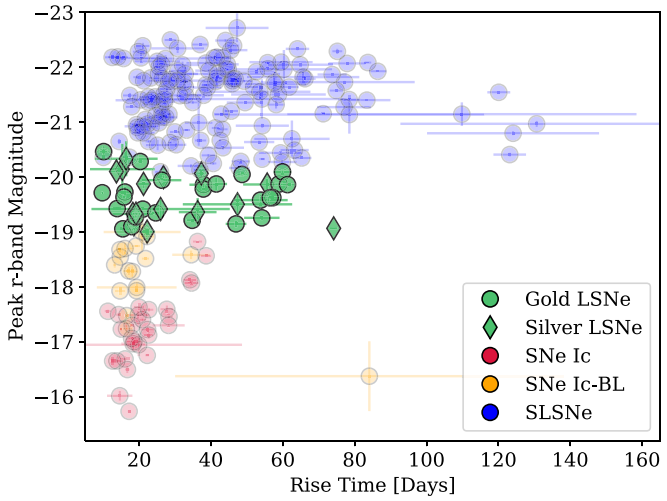

Figure 7. Rise time as a function of peak *r*-band absolute magnitude for the LSNe, SLSNe, SNe Ic, and SNe Ic-BL populations. We find that, by definition, LSNe occupy a very clear space in terms of peak magnitude, but they also have intermediate rise times between those of SLSNe and SNe Ic/Ic-BL.

5.3. Slow Ic-like

The LSNe in this group have red spectra like normal SNe Ic but light curves that are as broad as normal SLSNe (Figure 12). Six objects fall in this category: SN 2021ybf, DES16C3cv, SN 2021uvy, SN 2003L, SN 2019stc, and SN 2019cri. Unlike the previous two groups of Slow and Fast SLSN-like LSNe, the parameters of Slow Ic-like LSNe appear to bifurcate rather than cluster in a particular region of parameter space.

While the light curves of DES16C3cv, SN 2019cri, SN 2019stc, and SN 2021uvy are best fit by an almost pure magnetar model, SN 2003L and SN 2021ybf appear entirely radioactively powered. The only distinguishing feature is that the four magnetar-powered LSNe all show either a prominent secondary light-curve peak, or in the case of SN 2019cri, a late-time flattening that could be indicative of the start of a

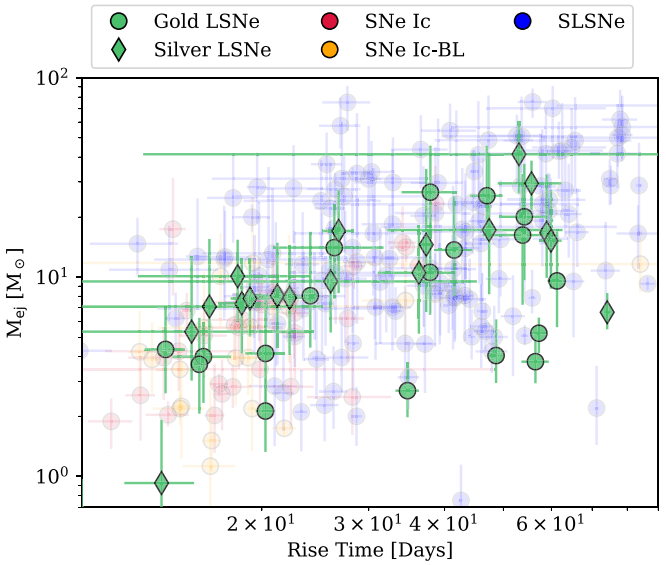

Figure 8. Ejecta mass as a function of rise time for the LSNe, SLSNe, SNe Ic, and SNe Ic-BL population. We see that, like previously established for SLSNe (e.g., Nicholl et al. 2015; Könyves-Tóth & Vinkó, 2021) and SNe Ic/Ic-BL (e.g., Dessart et al. 2016), LSNe with longer rise times tend to have larger ejecta masses.

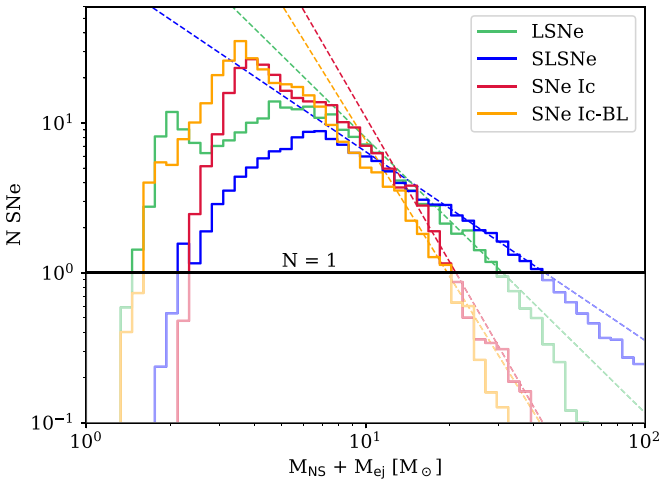

Figure 9. Pre-explosion mass distribution for the LSNe, SLSNe, SNe Ic, and SNe Ic-BL populations, normalized by their respective sample sizes. We estimate the progenitor mass by summing the best-fit value of the ejecta mass with the mass of the remnant neutron star. SLSNe have a sharp drop-off at the low-mass end, where SNe Ic peak, and LSNe are intermediate between these two populations. The same trend is seen in the high-mass end: SLSNe extend to very high masses of $\sim$40 $M_\odot$, LSNe appear to max out at $\sim$30 $M_\odot$, and SNe Ic/Ic-BL have almost no objects above $\sim$20 $M_\odot$. Dashed lines are linear fits to the distributions above 10 $M_\odot$ and below the $N = 1$ SN threshold. The peak in the LSNe distribution at $\sim$2 $M_\odot$ is driven entirely by two objects with tightly constrained M_{ej} values (iPTF16asu and SN 2021lwz).

secondary peak. Neither of the radioactively powered SNe show evidence for a secondary peak.

SN 2003L and SN 2021ybf have respective nickel mass fractions of $f_{Ni} \approx 0.12$ and $f_{Ni} \approx 0.08$, which explains why they are brighter than normal SNe Ic, which tend to have values of $f_{Ni} \lesssim 0.04$. Additionally, their respective high ejecta masses of $M_{ej} \approx 17$ $M_\odot$ and $M_{ej} \approx 20$ $M_\odot$ explain their slow evolution.

Conversely, DES16C3cv, SN 2019stc, SN 2021uvy, and SN 2019cri all appear magnetar dominated, but powered by

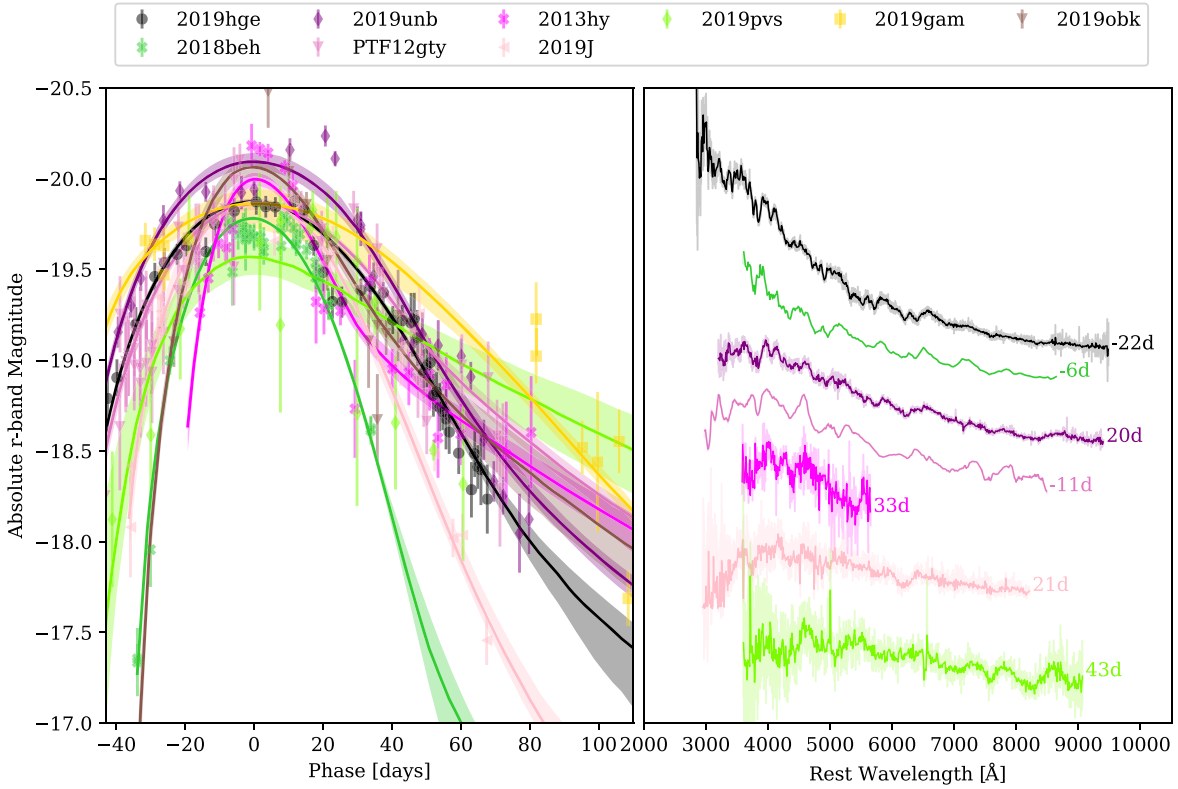

Figure 10. Light curves and spectra of the Slow SLSN-like LSNe group. Only *r*-band light curves and their respective MOSFiT models are shown. Spectra are arbitrarily scaled. Individual references are listed in Appendix A.

weaker magnetar engines than normal SLSNe. The first three have spin periods between 4 and 8 ms and magnetic fields between 4 and 8×10^{14} G, and SN 2019cri has a relatively high magnetic field of $\approx 6.5 \times 10^{14}$ G but a spin period of 13 ms, leading to its relatively low luminosity. We presented an in-depth analysis of SN 2019stc in Gomez et al. (2021), where we found the source to have an SLSN-like light curve, but a spectrum that is identical to those of normal SNe Ic. We concluded that a combination of radioactive decay and a magnetar central engine was required to power the luminous first peak while preserving a red Ic-like spectra. A similar interplay of power sources could be responsible for the luminous nature of these objects, while still preserving Ic-like spectra.

The LSNe in this group are divided into two groups. The SNe in one set (SN 2003L and SN 2021ybf) appear to be radioactively powered and are more luminous than normal SNe Ic due to their high nickel fractions, while their high ejecta masses lead to their slow evolution. The second set (DES16C3cv, SN 2019stc, SN 2021uvy, and SN 2019cri) are dominated by magnetars, but retain SNe Ic-like spectra. This could be a consequence of an interplay of power sources; while the magnetar component makes the SNe more luminous, the radioactive component makes the spectra appear Ic-like.

5.4. Fast Ic-like

This group is defined as LSNe with SN Ic-like spectra that also evolve rapidly, like SNe Ic, yet are significantly brighter than normal SNe Ic (Figure 13). This is the most populous group, with 12 SNe: iPTF13dnt, PTF11img, SN 2019uq, PS15cvn, SN 2019moc, SN 2021lei, SN 2019wpb, SN 2007ce, and SN 2010ay, SN 2018fcg, PTF10gvb, and iPTF17cw. We note that SN 2018fcg peaked at $M_r \sim -20.3$ mag and is technically outside the LSN definition, but we include it in the sample due to its strong spectral resemblance to normal SNe Ic and intermediate nature. These SNe have the slowest spin periods of all LSNe, with $P_{\rm spin} \gtrsim 15$ ms. For spin periods this slow, if the SNe have magnetars, these would have little to no contribution to the light curves. The main difference in terms of parameters between these SNe and normal SNe Ic is that these have significantly higher nickel mass fractions ($f_{\rm Ni} \gtrsim 0.07$) compared to the normal SNe Ic population ($f_{\rm Ni} \lesssim 0.04$). Two exceptions are PS15cvn and SN 2019uq, which both have nickel mass fractions $f_{\rm Ni} \lesssim 0.04$. SN 2019uq is a Silver LSN with poor photometric coverage, the dimmest object in this group, and possibly just a normal SN Ic. On the other hand, PS15cvn is the third brightest object in this group, likely due to its relatively high nickel mass of $M_{\rm Ni} \approx 0.15\,M_\odot$.

These LSNe are the most similar to normal SNe Ic in terms of power sources, light-curve durations, and spectral properties. These SNe can therefore be considered to be the brightest SNe Ic, where their high luminosity is due to an overabundance of nickel.

5.5. Other Objects

Some LSNe do not neatly fit into any of the previous four groups, and we include them here. There are six SNe in this group: SN 2019dwa, SN 2018don, SN 2019stc, PTF11hrq, OGLE15xl, and PTF12hni (Figure 14). The classification of these SNe is uncertain, either due to a lack of data, or because their nature is intermediate to two of the four groups presented here.

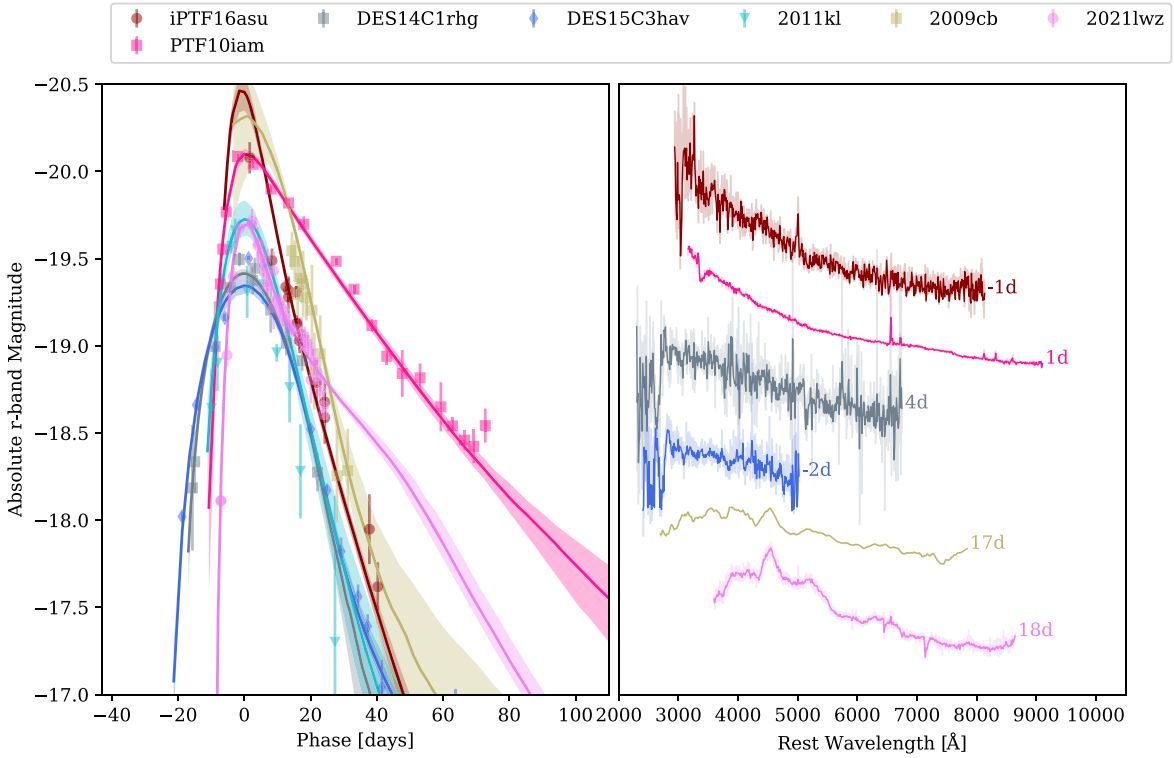

Figure 11. Light curves and spectra for the Fast SLSN-like LSNe group. Only *r*-band light curves and their respective MOSFiT models are shown. Spectra are arbitrarily scaled. Individual references are listed in Appendix A.

First is OGLE15xl, its light-curve fits are of poor quality due to the fact only one band is available, and its spectrum lies in between that of SLSNe and SNe Ic.

SN 2019dwa and PTF12hni are intermediate in every sense. Both objects have spectra intermediate to SLSNe and SNe Ic; bluer than normal SNe Ic but not quite as much as normal SLSNe. Both SNe also have an intermediate light-curve evolution. Therefore, these do not easily fit into any of the defined groups. Quimby et al. (2018) reached the same conclusion regarding the classification of PTF12hni.

SN 1991D is not spectroscopically similar to any other LSN, since it has clear evidence for helium in its spectra and was previously classified as a Type Ib SN by Benetti et al. (2002). SN 2012aa is another peculiar object in this category, which although lacking in helium, was previously identified by Yan et al. (2017) to have late-time signatures of hydrogen.

Finally, SN 2018don was presented in Lunnan et al. (2020) as an SLSN with possibly substantial host galaxy extinction of $A_V \approx 0.4$ mag. Correcting for this amount of extinction would place the SN well into the normal SLSN regime. Due to the uncertainty in the extinction value, we avoid grouping this object into one of the four groups.

5.6. Summary

In Figure 15 we show how the LSNe, now labeled in terms of their groupings, lie in the $B_\perp$ versus $P_{\rm spin}$ parameter space and how they compare to the SLSNe and SNe Ic/Ic-BL populations. We find that after grouping LSNe into distinct classes, some separation does begin to appear. Mainly, Slow SLSN-like LSNe seem to occupy mostly the same parameter space as SLSNe, having powerful magnetars; whereas Fast Ic-like LSNe overlap mostly with the existing SNe Ic population with weak or no evidence for magnetars. Slow Ic-like LSNe on the other hand, still span a wide range of parameter space. And Fast Ic-like LSNe have strong magnetic fields, but spin periods that are slow enough to make the magnetar contribution negligible. In conclusion, brighter objects tend to have SLSN-like spectra, while dimmer objects more closely resemble SNe Ic.

The different groups of LSNe separate well in terms of their rise time and peak luminosity. In Figure 16 we show that Fast SLSN-like LSNe have short rise times and high peak luminosities, Fast Ic-like LSNe also have short rise times but with low peak luminosities, Slow SLSN-like LSNe have long rise times and high peak luminosities, and finally, Slow Ic-like LSNe have long rise times but low peak luminosities. In the same plot, we can see that all objects with a double-peaked light curve lie in the quadrant with slow rise times and high peak luminosities. And all the objects that show possible helium are among the brighter LSNe, most of them also having long rise times.

6. Observational Properties

6.1. Spectral Features

We explore the presence of helium in LSNe and find that SN 1991D, SN 2003L, SN 2019gam, SN 2019hge, SN 2019obk, SN 2019unb, SN 2018beh, and SN 2018fcg show tentative evidence for helium in their spectra. These SNe are all brighter than $M_r \sim -19.5$ mag and have rise times spanning $\sim$15 to $\sim$60 days. Yan et al. (2020) presented a sample of seven SLSNe with possible detections of helium, three of which had peak magnitudes $M_r \lesssim -20.5$ mag and are therefore outside the definition of LSNe, the remaining four (SN 2019gam, SN 2019hge, SN 2019unb, and SN 2019obk) all lie in the Slow SLSN-like LSNe group. The excitation of

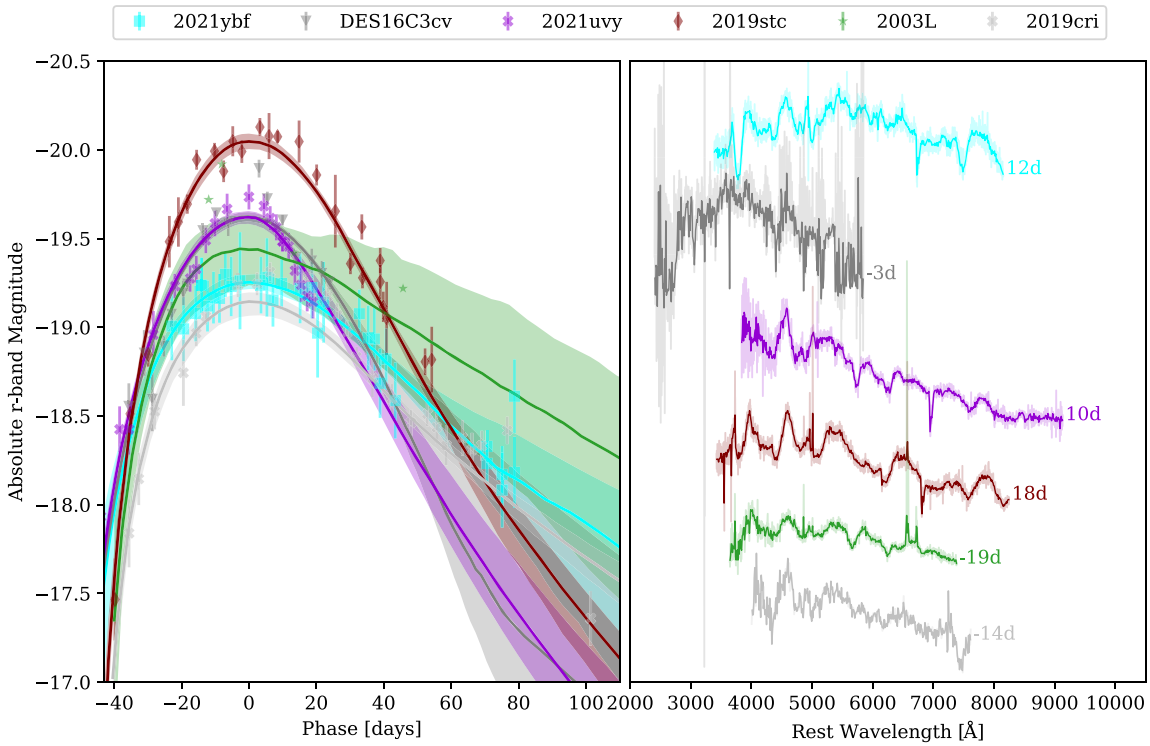

Figure 12. Light curves and spectra of the Slow Ic-like LSNe group. Only *r*-band light curves and their respective `MOSFiT` models are shown. Spectra are arbitrarily scaled. Individual references are listed in Appendix A.

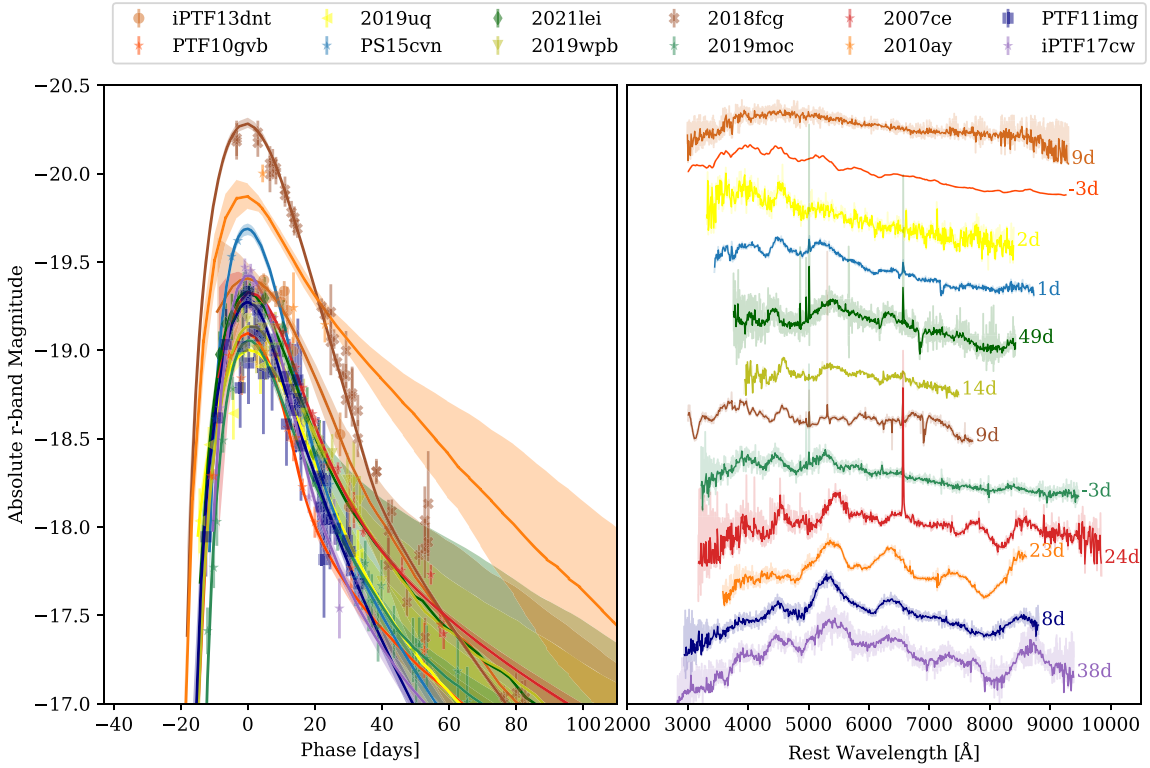

Figure 13. Light curves and spectra of the Fast Ic-like LSNe group. Only *r*-band light curves and their respective `MOSFiT` models are shown. Spectra are arbitrarily scaled. Individual references are listed in Appendix A.

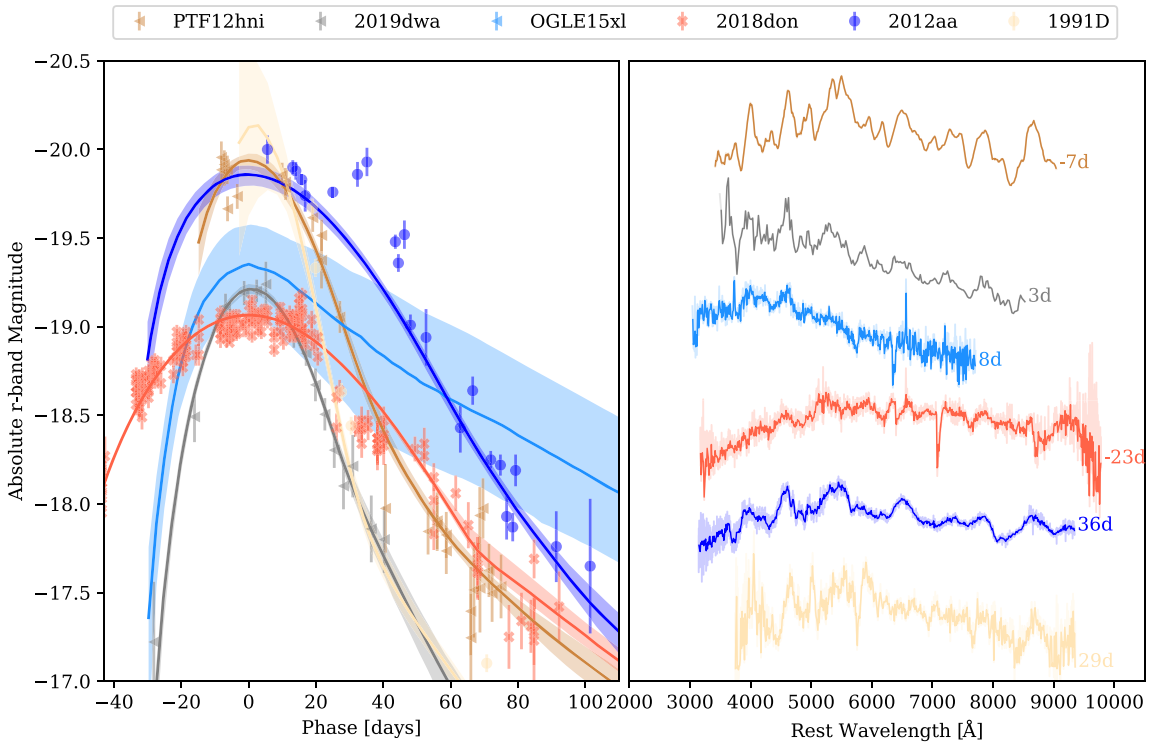

Figure 14. Light curves and spectra of the Other group. Only *r*-band light curves and their respective `MOSFiT` models are shown. Spectra are arbitrarily scaled. Individual references are listed in Appendix A.

helium in SLSNe requires either nonthermal radiation, potentially from a magnetar central engine (Dessart et al. 2012), or interaction with helium-rich circumstellar material (Yan et al. 2015).

SLSNe tend to show a broad W-shaped absorption feature found around 4200 and 4450 Å not seen in SNe Ic (Quimby et al. 2018). We find that no LSN has this distinctive O II W-shaped line, which could simply be a result of these SNe not reaching sufficiently high temperatures at early time to excite these ions or very rapid cooling of the ejecta.

6.2. Double-peaked Light Curves

Four LSNe (SN 2019stc, DES16C3cv, SN 2021uvy, and SN 2019hge) show a double-peaked light-curve structure. All four are relatively bright with magnitudes $M_r \lesssim -19.5$ mag, and have rise times greater than ∼45. SN 2019hge is the only LSN that shows both a double-peaked structure and the presence of helium. The interplay between the distinct power sources of radioactive decay and a magnetar engine may be responsible for the double-peaked structure observed in some LSNe.

6.3. Relative Rates

Given the fact that we selected the population of LSNe presented here from nonuniform surveys, we can not draw definitive conclusions regarding their absolute rate. Nevertheless, we can estimate their relative rates. We apply a volumetric correction to the population of LSNe, SLSNe, and SNe Ic/Ic-BL to account for Malmquist bias following the method of De Cia et al. (2018) and find that LSNe are more common than SLSNe but less common than either SNe Ic or SNe Ic-BL.

We compare our sample of LSNe to the ZTF Bright Transient Survey (BTS; Perley et al. 2020) to estimate their observational rates. The BTS aims to spectroscopically classify every bright transient found by ZTF, with a completeness of ∼93% down to 18.5 mag. At the time of comparison, the BTS[11] list of SN-like events has 3636 objects brighter than $m_r = 19$ mag, which have already been pruned to only include SN-like objects with well-sampled light curves and low extinction $A_V < 1$ mag. We find that LSNe are rare, making up only $0.3\% \pm 0.1\%$ of SN-like transients from the BTS survey, or $0.4\% \pm 0.1\%$ of all CCSNe observed by this magnitude-limited survey. For comparison, SLSNe make up ∼1% of all the SN-like transients in the BTS survey.

7. Conclusions

We have presented the first comprehensive study of all the stripped-envelope CCSNe that lie in the intermediate regime between SLSNe and SNe Ic, allowing us to better place SLSNe in the context of CCSNe, how they relate to other SNe, and the nature of their progenitors. We analyzed a sample of 40 LSNe, defined as stripped-envelope CCSNe with a peak *r*-band magnitude between $M_r = -19$ and -20 mag, bounded by SLSNe on the bright end, and by SNe Ic/Ic-BL on the dim end. Observationally, we find that:

1. LSNe have intermediate rise times between ≈20 and 65 days.

[11] https://sites.astro.caltech.edu/ztf/bts/bts.php

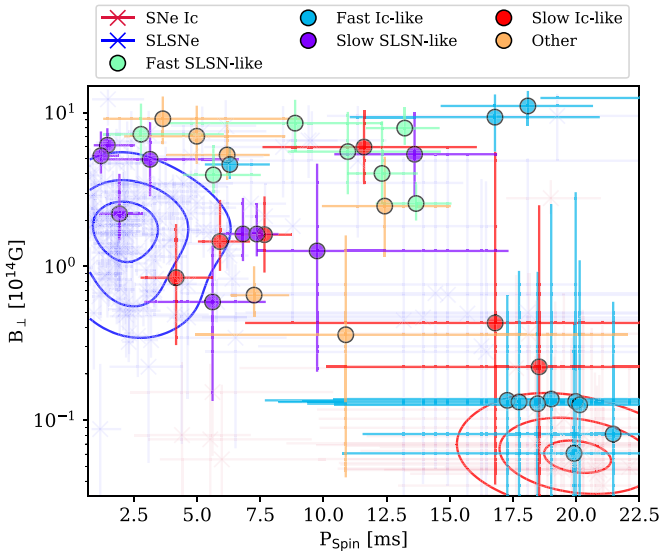

Figure 15. Same as Figure 4, but with LSNe labeled based on their distinct groups. We see that LSNe do not perfectly separate into distinct classes, even after subdividing them. But some trends so start to appear: Slow SLSN-like LSNe mostly reside in the SLSNe-dominated parameter space; Fast Ic-like LSNe mostly overlap with the existing SNe Ic population; Fast SLSN-like and Slow Ic-like LSNe lie outside the typical parameter space occupied by SLSNe or SNe Ic.

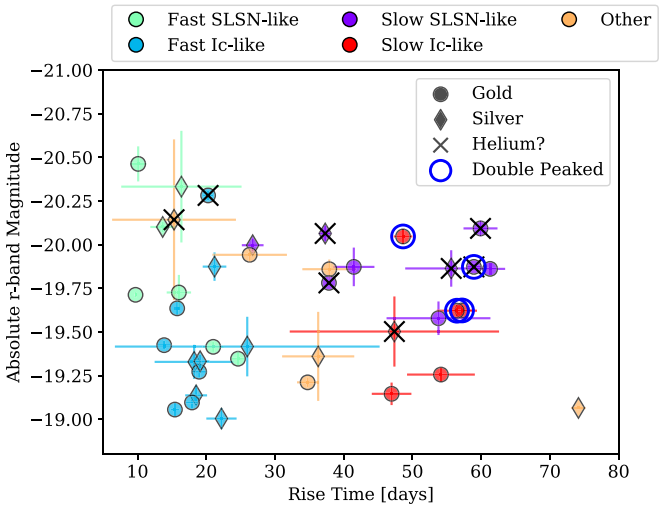

Figure 16. Peak *r*-band magnitude as a function of rise time for LSNe, labeled by their distinct groupings. We see that LSNe do appear to separate well in terms of rise time and absolute peak magnitude, forming four distinct quadrants.

2. The spectra of LSNe span a continuum, from blue and SLSN-like to red and SNe Ic-like.
3. Brighter LSNe tend to have SLSN-like spectra, while dimmer LSNe resemble SNe Ic.
4. No LSN shows the distinctive W-shaped O II absorption feature found in some SLSNe.
5. LSNe are rare and make up ∼0.3% of all SNe-like transients from a magnitude-limited survey; or ∼0.4% of all observed CCSNe.
6. In absolute terms, LSNe are likely more common than SLSNe, but less common than SNe Ic/Ic-BL.
7. LSNe with possible helium are brighter than ∼−19.5 mag.
8. LSNe with a double-peaked light curve are brighter than ∼−19.5 mag and have long rise times $\gtrsim$45 days.

We modeled the light curves of all 40 LSNe, as well as a sample of 149 SLSNe and 61 SNe Ic/Ic-BL in a uniform way with a combined magnetar plus radioactive decay model to compare their physical parameters. From our models we find that:

1. Around 25% of LSNe appear to be radioactively powered, while the rest have at least a 50% contribution from a magnetar engine.
2. The nickel fractions for the radioactively dominated LSNe span a range of $f_{\rm Ni} \approx 0.01$–0.1, similar to SNe Ic/Ic-BL.
3. The pre-explosion masses of LSNe extend to ∼30 $M_\odot$, higher than SNe Ic/Ic-BL, but not as high as SLSNe. The slope of the high-end mass distribution of LSNe is also intermediate to SLSNe and SNe Ic/Ic-BL, as is the peak of their distribution.
4. The pre-explosion masses of LSNe can be as low as those of SNe Ic/Ic-BL, ∼1.5 $M_\odot$.
5. Like SLSNe and SNe Ic/Ic-BL, LSNe with larger ejecta masses have longer rise times.

We attempt to separate LSNe into distinct groups and find a natural breakdown in terms of their spectral similarity to either SLSNe or SNe Ic, and whether their light curves evolve fast like SNe Ic or slowly like SLSNe. We present four main groups of LSNe: Slow SLSN-like, Fast SLSN-like, Slow Ic-like, and Fast Ic-like. From these subgroups, we find that:

1. Slow SLSN-like LSNe are the most similar to normal SLSNe. They are less luminous due to their slow spin periods, and long lasting due to their large ejecta masses. These are effectively the lowest luminosity SLSNe known.
2. Fast SLSN-like LSNe evolve rapidly due to their low ejecta masses, but their strong magnetars make them more luminous than normal SNe Ic.
3. Slow Ic-like LSNe bifurcate into two groups: a population of radioactively powered SNe with higher nickel fractions than typical SNe Ic/Ic-BL; and a magnetar-powered population with magnetars weaker than normal SLSNe, and spectra that still resemble SNe Ic likely due to the presence of radioactive decay.
4. Fast Ic-like LSNe are the most similar to normal SNe Ic but are more luminous due to their relatively high nickel fractions and masses. These can be considered the most luminous SNe Ic known.

We have shown that some LSNe are an extension toward either the dimmest SLSNe (Slow SLSN-like LSNe) or the brightest SNe Ic known (Fast Ic-like LSNe), while other LSNe appear to have a more complex nature, borrowing a combination of properties from SLSNe and SNe Ic. We have analyzed in a systematic way all the SNe that occupy the up to now mostly unexplored link between SLSNe and SNe Ic. This work opens the door for subsequent studies that will focus on the details of the spectroscopic features of LSNe and how they relate to SLSNe and SNe Ic, as well as an in-depth study of their host galaxies and environments. Looking further ahead, the Legacy Survey of Space and Time (Ivezić et al. 2019), scheduled to commence in 2023, will increase the transient discovery rate by about 2 orders of magnitude, and will allow us to explore the cutting edges of parameter space, providing a

more comprehensive view of the relation between various types of CCSNe.

We thank Y. Beletsky for carrying out some of the Magellan observations. S.G. is partly supported by an STScI Postdoctoral Fellowship. The Berger Time-Domain Group at Harvard is supported by NSF and NASA grants. M.N. is supported by the European Research Council (ERC) under the European Union's Horizon 2020 research and innovation program (grant agreement No. 948381) and by a Fellowship from the Alan Turing Institute. This paper includes data gathered with the 6.5 m Magellan Telescopes located at Las Campanas Observatory, Chile. Observations reported here were obtained at the MMT Observatory, a joint facility of the University of Arizona and the Smithsonian Institution. This research has made use of NASA's Astrophysics Data System. This research has made use of the SIMBAD database, operated at CDS, Strasbourg, France. IRAF is written and supported by the National Optical Astronomy Observatories, operated by the Association of Universities for Research in Astronomy, Inc. under cooperative agreement with the National Science Foundation. Operation of the Pan-STARRS1 telescope is supported by the National Aeronautics and Space Administration under grant No. NNX12AR65G and grant No. NNX14AM74G issued through the NEO Observation Program. This work has made use of data from the European Space Agency (ESA) mission Gaia (https://www.cosmos.esa.int/gaia), processed by the Gaia Data Processing and Analysis Consortium (DPAC, https://www.cosmos.esa.int/web/gaia/dpac/consortium). Funding for the DPAC has been provided by national institutions, in particular the institutions participating in the Gaia Multilateral Agreement. This work makes use of observations from Las Cumbres Observatory global telescope network.

Facilities: ADS, TNS.

Software: Astropy (Astropy Collaboration et al. 2018), extinction (Barbary 2016), Matplotlib (Hunter 2007), emcee (Foreman-Mackey et al. 2013), NumPy (van der Walt et al. 2011), FLEET (Gomez et al. 2020b), MOSFiT (Guillochon et al. 2018), PyRAF (Science Software Branch at STScI 2012), SAOImage DS9 (Smithsonian Astrophysical Observatory 2000), corner (Foreman-Mackey 2016), HOTPANTS (Becker 2015), SciPy (van der Walt et al. 2011), PYPHOT (https://github.com/mfouesneau/pyphot).

Appendix A

In Table 5 we list all the new previously unpublished spectra used in this work. In Table 6 we list all the photometry used for this work, both previously published and new.

We provide a list of all the LSNe used for this work, separated into groups. First, a confident sample of Gold LSNe (Appendix B) that have good photometric and spectroscopic coverage. Then, a list of Silver LSNe (Appendix C), objects that either have some missing data. Both the Gold and Silver groups were used for all our analyses. Then, we list a sample of Bronze LSNe (Appendix D); objects that are either severely lacking in data. For completeness, we provide a list of peculiar objects that even though they meet the luminosity threshold for LSNe, are very distinct in nature and likely unrelated to LSNe (Appendix E). Finally, we list the Type Ic and Ic-BL SNe used for comparison in this work (Appendix F).

Table 5
Log of Optical Spectroscopic Observations

Supernova	UT Date	Phase (days)	Exposure Time (s)	Instrument + Telescope
SN 2018fcg	2018 Sep 8	+9	1200	Blue Channel + MMT
SN 2019pvs	2019 Nov 4	+43	1500	LDSS3c + Magellan
SN 2021lei	2021 Jul 7	+49	2700	IMACS + Magellan
SN 2021lwz	2021 Jun 6	+18	1500	Binospec + MMT
SN 2021uvy	2021 Sep 7	+10	1620	LDSS3c + Magellan
SN 2021ybf	2021 Oct 7	+12	2700	Binospec + MMT

Table 6
Log of Photometric Observations

Supernova	MJD	Mag	Raw	MagErr	Telescope	Instrument	Filter	UL	System	Ignore	Source
2021uvy	59606.082031	20.0442	20.2629	0.06620	FLWO	KeplerCam	*g*	False	AB	False	This work
2021uvy	59606.085937	19.9689	20.1264	0.06510	FLWO	KeplerCam	*r*	False	AB	False	This work
2021uvy	59606.093750	20.1336	20.2547	0.09170	FLWO	KeplerCam	*i*	False	AB	False	This work
2021uvy	59609.085937	20.0729	20.2916	0.06770	FLWO	KeplerCam	*g*	False	AB	False	This work
2021uvy	59609.093750	20.0595	20.2170	0.05790	FLWO	KeplerCam	*r*	False	AB	False	This work
2021uvy	59609.101562	20.4580	20.5790	0.12510	FLWO	KeplerCam	*i*	False	AB	False	This work

Note. Sample of table format, the full table available in machine-readable format. For each SN we provide the MJD, the Mag (corrected for galactic extinction and in some cases host flux contribution), the Raw magnitude without such corrections, The magnitude error MagErr, the telescope, instrument, and band used, as well as whether or not the measurement is an Upper Limit. We also include an "Ignore" column on whether or not we excluded the data for the `MOSFiT` model. Source indicates the source of the photometry calculations, not necessarily the source of the original images.

(This table is available in its entirety in machine-readable form.)

Appendix B
Gold LSNe

B.1. 2011kl

SN 2011kl (=GRB111209A) was classified as an SLSN-I with an associated GRB by Greiner et al. (2015), the authors determine a redshift of $z = 0.677$ based on afterglow spectra. Their photometry is corrected for the GRB afterglow contribution, host extinction, galactic extinction, and host galaxy flux. The resulting light curve is brighter than normal SNe Ic, but not quite in the regime of SLSNe, consistent with the conclusions of Kann et al. (2019). Mazzali et al. (2016) also classify the spectra as an SLSN-I.

B.2. 2012aa

SN 2012aa (=PSN J14523348-0331540 = Howerton-A20) was presented by Roy et al. (2016) as an SN in between a Type Ibc and an SLSN-I. We include two early photometry points from the CRTS that Roy et al. (2016) calibrate to the V band. We subtract a nominal magnitude of $m_V = 19.11$ mag from those data to account for the host flux. Including spectra from Shivvers et al. (2019), we agree with the peculiar spectral classification and find that SN 2012aa is overall a good spectral match to SNe Ic-BL, but also shares some similarities with the SLSN-I 2016wi, both showing late-time signs of hydrogen Yan et al. (2017).

B.3. 2018beh

SN 2018beh (=ZTF18aahpbwz = ASASSN-18ji = PS18ats = ATLAS18nvb) was classified as an SN Ib/c by Mcbrien et al. (2018) and as an SN Ic by Dahiwale & Fremling (2020a). We include one upper limit from ATLAS and one from ASAS-SN. We include our own PSF photometry of FLWO, LCO, and ZTF images after doing difference imaging to subtract the host flux. We exclude detections before MJD = 58212 from the MOSFiT fit, since these seem to be from a pre-explosion feature. The spectra match that of an SLSN-I at early times. The light curve is dim for an SLSN-I. Comparison spectra are from the TNS (Mcbrien et al. 2018; Dahiwale & Fremling 2020a).

B.4. 2018fcg

SN 2018fcg (=ZTF18abmasep = Gaia18cms = ATLAS18ucc) was classified as an SLSN-I by Fremling et al. (2018a) and Lunnan et al. (2018). We include photometry from Gaia, ATLAS, and ZTF. In addition, we include our own PSF photometry of FLWO images after doing difference imaging to subtract the host flux. We do not include photometry from Hernandez-Garcia et al. (2018), since these are not corrected for the host flux. We exclude the r-band points from ZTF after MJD = 58420 since they are very discrepant from all other sources of photometry. Our own spectra of SN 2018fcg from the Blue Channel and Binospec spectrographs are more consistent with an SN Ic spectrum, yet the light curve is most similar to fast SLSN-like LSNe.

B.5. 2019cri

SN 2019cri was classified as an SN Ic by Fremling et al. (2019a) and Prentice et al. (2019b). The spectra look like an SN Ic, but the light curve is much broader than typical SNe Ic, closer to the broadness of SLSN-I. We include photometry from ATLAS, Gaia, PS1, and ZTF. Comparison spectra were obtained from the TNS (Fremling et al. 2019a; Prentice et al. 2019b). This object was presented as the equivalent of an LSN in Prentice et al. (2021).

B.6. 2019dwa

SN 2019dwa (=ZTF19aarfyvc = Gaia19bxj) was classified as an SN Ic by Fremling et al. (2019d). We include photometry from the GSA and ZTF. Fremling et al. (2019d) report a redshift of $z = 0.09$, but we find a redshift of $z = 0.082$ to be a better match to the SN features. The spectra are consistent with either particularly blue SNe Ic or particularly red SLSN-I. The light curve is as bright as the brightest normal SNe Ic, but broader. The comparison spectrum was obtained from the TNS (Fremling et al. 2019d). This object was presented as the equivalent of an LSN in Prentice et al. (2021).

B.7. 2019hge

SN 2019hge (=ZTF19aawfbtg = Gaia19est = ATLAS19och = PS19elv) was classified as an SLSN-Ib by Yan et al. (2020). We include photometry from ZTF, PS1, and the GSA. But we exclude the photometry after MJD = 58650 from the MOSFiT fit, since the SN shows a late-time re-brightening, which effectively removes all the GSA data from the fit. The spectra match those of SLSN-I. This object is only marginally dimmer than most SLSN-I, and could be just a dim SLSN-I with possible helium. Additional comparison spectra are from Dahiwale et al. (2019a) and Prentice et al. (2019c). This object was presented as the equivalent of an LSN in Prentice et al. (2021).

B.8. 2019J

SN 2019J (=ZTF19aacxrab = PS18crs = ATLAS19cay) was classified as an SLSN-I by Fremling et al. (2019b). We include photometry from PS1, ATLAS, and our own PSF photometry of ZTF images after doing difference imaging to subtract the host flux. The spectra match an SLSN-I, but the light curve is dim for an SLSN-I. The comparison spectrum was obtained from the TNS (Fremling et al. 2019b).

B.9. 2019moc

SN 2019moc (=ZTF19ablesob = Gaia19dks = ATLAS19rgu) was classified as an SN Ic-BL by Dahiwale et al. (2019b) and as an SN Ic by Nicholl et al. (2019). We include photometry from ZTF, Gaia, and ATLAS. This source is only marginally in the LSNe range with a peak absolute magnitude of $M_r = 19.1$ mag and has an overall close resemblance to a normal SN Ic.

B.10. 2019pvs

We classified SN 2019pvs (=ZTF19abuogff = PS19fbe) as an SLSN-I as part of FLEET (Gomez et al. 2021). We determine a redshift of $z = 0.167$ based on host emission lines. We include photometry from PS1, and our own PSF photometry of FLWO and ZTF images after doing difference imaging to subtract the host flux. The light curve is as broad as normal SLSN-I, but dimmer. The late-time spectra match either an SLSN-I or an SN Ic. We include two spectra of SN 2019pvs we obtained with the LDSS spectrograph.

B.11. 2019stc

We classified SN 2019stc (=ZTF19acbonaa) as a transitional object between an SLSN-I and an SN Ic; having an SN Ic spectrum but light-curve features and environment resembling an SLSN-I (Gomez et al. 2021). The light curve shows a pronounced second peak, we include photometry up to MJD = 58853 (excluding the secondary peak) and spectra from Gomez et al. (2021). Yan et al. (2020) classified SN 2019stc as an SLSN-I.

B.12. 2019unb

SN 2019unb (=ZTF19acgjpgh = Gaia19fbu = PS19isr = ATLAS19bari) was classified as an SLSN-Ib by Yan et al. (2020). We include photometry from ZTF, the GSA, PS1, and ATLAS. This object is only marginally dimmer than most SLSN-I, and could be just a dim SLSN-I with possible helium. Comparison spectra are from Prentice et al. (2019a) and Dahiwale & Fremling (2020b). This object was presented as the equivalent of an LSN in Prentice et al. (2021).

B.13. 2021lwz

SN 2021lwz was classified as an SLSN-I by Perley et al. (2021). The spectra are blue and SLSN-I like, but also share features with normal SNe Ic. The peak magnitude is dimmer than typical SLSNe. We include photometry from ZTF, ATLAS, and our own PSF photometry of FLWO images. Comparison spectra are from Perley et al. (2021).

B.14. 2021uvy

SN 2021uvy was classified as an SLSN-I by Poidevin et al. (2021), as an SN Ib/c by Ridley et al. (2021), and as a peculiar SN Ib by Chu et al. (2021). We include photometry from ZTF. We find the spectra are a good match to SNe Ib/c. The light curve of this object has a pronounced second peak begging at MJD = 59476, which we exclude from the MOSFiT fit. We include two spectra we obtained with the Binospec spectrograph on MMT and the LDSS3c spectrographs.

B.15. 2021ybf

SN 2021ybf was classified as an SLSN-I by Bruch et al. (2021). We include photometry from ZTF. We obtained spectra of the source with the Binospec spectrograph and find it to be most consistent with an SN Ic, the peak luminosity is also similar to SNe Ic. Nevertheless, the light curve is much broader than for typical SNe Ic.

B.16. DES14C1rhg

DES14C1rhg was classified as a Gold SLSN-I by Angus et al. (2019). We include photometry and spectra from Angus et al. (2019), but exclude detections before MJD = 56990 from the MOSFiT fit since the SN shows a slow pre-brightening. The spectra are noisy but broadly consistent with an SLSN-I. The light curve is slightly brighter and broader than a normal SN Ic.

B.17. DES15C3hav

DES15C3hav was classified as a Gold SLSN-I by Angus et al. (2019). We include photometry and spectra from Angus et al. (2019), but exclude detections before MJD = 57305 from the MOSFiT fit since these are due to a particularly red pre-SN feature. The spectra are noisy but broadly consistent with an SLSN-I. The light curve is slightly brighter and broader than a normal SN Ic.

B.18. DES16C3cv

DES16C3cv was classified as a Silver SLSN-I by Angus et al. (2019). We include photometry from Angus et al. (2019), which has a very pronounced second peak. We exclude the first *i*-band point from the MOSFiT model since this is inconsistent with the rest of the light-curve rise. We also impose a conservative cut and remove data after MJD = 57720 from the fit to exclude the second peak from the fit. The spectrum of DES16C3cv was taken near the first peak when SLSNe tend to be very blue. Despite the spectrum being quite noisy, it does not appear particularly blue but is rather consistent with an SN Ic spectrum.

B.19. iPTF16asu

iPTF16asu was classified as an SLSN-I by Whitesides et al. (2017). The authors correct the photometry for extinction using $E(B-V) = 0.029$ and report all magnitudes in the AB system. The early spectra match an SLSN-I, yet the late-time spectra match those of SNe Ic-BL. The light curve reaches a peak magnitude close to those of SLSN-I, but the decline is very fast, similar to SNe Ic. This object was included in the SNe Ic-BL sample from Taddia et al. (2019).

B.20. iPTF17cw

iPTF17cw was classified as an SN Ic-BL by Taddia et al. (2019). The spectra at late times resemble SNe Ic-BL, yet at early times the spectra are bluer than normal SNe Ic. The light curve is on the bright end for SNe Ic. We include photometry and spectra from Taddia et al. (2019).

B.21. PS15cvn

PS15cvn (=MLS151203:000922-000407 = iPTF15dqg) was classified as an SN Ic by Kangas et al. (2015) and then reclassified as an SN Ic-BL by Taddia et al. (2019). We include photometry from PS1, the CRTS, and Taddia et al. (2019). The spectra match an SN Ic-BL and are a good match to SN 2007ce Quimby et al. (2007). The peak magnitude of the light curve is in between those of SLSN-I and SNe Ic. Spectra are from Taddia et al. (2019).

B.22. PTF10gvb

PTF10gvb was classified as a possible SLSN-I by Quimby et al. (2018), who noted the spectra are consistent with either an SLSN-I or an SN Ic-BL. The host was studied in Taggart & Perley (2021). The source was presented as an SN Ic-BL in the Taddia et al. (2019) sample. We include photometry from Taddia et al. (2019). The light curve of PTF10gvb resembles a normal SN Ic. This object is only marginally in the LSNe range, with a peak absolute magnitude of $M_r = -19.0$. Most

evidence points toward PTF10gvb being a slightly luminous but otherwise normal SN Ic-BL.

B.23. PTF11img

PTF11img was classified as an SN Ic-BL by Taddia et al. (2019), but its peak magnitude is within the LSNe range. We include photometry from Taddia et al. (2019).

B.24. PTF12gty

PTF12gty was classified as an SLSN-I by Quimby et al. (2018). Barbarino et al. (2020) classified PTF12gty as an SN Ic due to the similarity in spectral features. We argue the spectrum is closer to an SLSN-I, despite sharing some features with early SNe Ic. The light curve of PTF12gty is as bright and broad as dim SLSN-I. We include photometry from De Cia et al. (2018), which the authors correct for extinction using $E(B-V)=0.058$. Comparison spectra are from Quimby et al. (2018).

B.25. PTF12hni

PTF12hni was classified as an SLSN-I by Quimby et al. (2018). We include photometry from De Cia et al. (2018), which the authors correct for extinction using $E(B-V)=0.052$. The SN shows a re-brightening after ∼75 days, which is why we exclude detections after MJD = 56250 from our MOSFiT fit. The features of the spectrum are consistent with an SLSN-I, but redder than normal SLSN-I and closer to SNe Ic. The shape of the light curve is in between those of SLSN-I and SNe Ic. Comparison spectra are from Quimby et al. (2018).

Appendix C
Silver LSNe

C.1. 1991D

SN 1991D was classified as a luminous SN Ib by Benetti et al. (2002). We adopt a redshift of $z=0.04179$, established from a spectrum of the host galaxy (Maza & Ruiz 1989). At this redshift, the peak magnitude of the SN is $M_R\sim-19.7$, much brighter than normal SNe Ib. We include photometry from Benetti et al. (2002) and spectroscopy from Matheson et al. (2001). The spectra at late times resemble those of SLSNe, with strong spectral similarities to the LSN 2019pvs. Unlike SN 2019pvs, SN 199D has a much narrower light curve, fading by 2 mag in under ∼20 days. Moreover, SN 199D has strong helium lines, much like the SLSN-Ib sample from Yan et al. (2020), despite fading much faster than these. We assign a Silver label due to the lack of photometry during the rise or peak of the light curve, which prevents us from accurately estimating its peak magnitude and physical parameters. This also means that the peak date might have been much earlier than estimated.

C.2. 2003L

SN 2003L was classified as an SN Ic by Valenti et al. (2003) and reported in Soderberg et al. (2005) as an SN Ibc. At the time, SN 2003L was the second-most luminous SN Ib/c discovered, just after SN 1998bw. We include photometry from the CRTS and the VSNET (Nogami et al. 1997). The optical spectra obtained from Shivvers et al. (2019) resemble that of an SN Ib, with clear helium lines, but the light curve is much broader and brighter than normal SNe Ib. We assign a Silver label due to the very sparse light curve.

C.3. 2007ce

SN 2007ce was classified as an SN Ic by Quimby et al. (2007) and reclassified in Modjaz et al. (2014) as an SN Ic-BL. We include photometry from Bianco et al. (2014). The spectra from Modjaz et al. (2014) and Shivvers et al. (2019) mostly match SNe Ic-BL spectra, but also resemble the spectra of the SLSN-I 2018avk Lunnan et al. (2020). We assign a Silver label due to the very sparse light curve and lack of coverage during the light-curve peak.

C.4. 2009cb

SN 2009cb (=CSS090319:125916+271641 = PTF09as) was classified as an SLSN-I by Quimby et al. (2018). We adopt a redshift of $z=0.1867$, determined from a study of the host galaxy by Perley et al. (2016), who found a redshift of $z=0.1867$. We use photometry from De Cia et al. (2018), which the authors correct for extinction using $E(B-V)=0.0065$. We assign a Silver label since the SN was caught after peak, so there is no photometry available during the rise of peak, but our MOSFiT model predicts a peak magnitude of $M_r\sim-20$ mag, within the range of SLSNe. The spectra match either an SN Ic or an SLSN-I, but given the uncertainty in the peak date, we might be underestimating the phase, which would make an SLSN-I classification more plausible.

C.5. 2010ay

SN 2010ay (=CSS100317:123527+270403) was classified as an SNe Ic-BL by Sanders et al. (2012), who noted this was one of the most luminous SNe Ib/c ever discovered. We only include photometry from Sanders et al. (2012). Additional spectra from Shivvers et al. (2019) also resemble SNe Ic-BL. We assign a Silver label due to the very sparse light curve and lack of photometry during the rise.

C.6. 2013hy

SN 2013hy (=DES13S2cmm) was classified as an SLSN-I by Papadopoulos et al. (2015) and as a Gold SLSN-I by Angus et al. (2019). Ouyed et al. (2015) argue SN 2013hy was actually a quark nova in a high-mass X-ray binary. We only include photometry from Angus et al. (2019). The light curve is almost as bright as normal SLSNe, but evolves as fast as SNe Ic. The spectra have a very low signal-to-noise ratio (S/N), but overall match the shape and general features match those of SLSN-I. We assign a Silver label due to the poor spectral coverage from a single low S/N spectrum.

C.7. 2018don

SN 2018don (=ZTF18aajqcue = PS18aqo) was classified as an SLSN-I by Lunnan et al. (2020), but noting this could also be an SN 2007bi-like event with considerable reddening, or a long-lived and luminous SN Ic. The authors correct the photometry for foreground extinction using $E(B-V)=0.009$, but find a total extinction of $E(B-V)=0.4$ when accounting for the intrinsic host extinction. We include photometry from Lunnan et al. (2020) and additional photometry from PS1,

which we correct for extinction by the same value of $E(B-V)=0.009$. Additional spectra from Fremling et al. (2019e) are consistent with SNe Ic. The light curve is as broad as normal SLSN-I, but much dimmer, may be a consequence of the strong reddening. We assign a Silver label due to the uncertainty in the extinction value, which could be very high, making this a normal SLSN-I.

C.8. 2019gam

SN 2019gam (=ZTF19aauvzyh = ATLAS19lsz) was classified as an SLSN-Ib/IIb by Yan et al. (2020). We include photometry from ATLAS and our own PSF photometry of ZTF images after doing difference imaging to subtract the host flux. This object is only marginally dimmer than most SLSN-I, and could be just a dim SLSN-I with possible helium. We assign a Silver label since there is no photometry coverage during peak and the spectral data are not available for download, preventing further spectral comparisons.

C.9. 2019obk

SN 2019obk (=ZTF19abrbsvm = PS19eqz = ATLAS19tvm) was classified as an SLSN-Ib by Yan et al. (2020). We include photometry from ATLAS and our own PSF photometry of ZTF images after doing difference imaging to subtract the host flux. We assign a Silver label since the spectral data are not available for download, preventing further spectral comparisons and our light-curve model is unable to reproduce the fast decline of the *r*-band light curve.

C.10. 2019uq

SN 2019uq (=ZTF19aadgqvd = ATLAS19bos) was classified as an SN Ic by Piranomonte et al. (2019). We include photometry from ATLAS and our own PSF photometry of ZTF images after doing difference imaging to subtract the host flux. The spectra are not a perfect match to normal SLSN-I, but instead match the peculiar SLSN-Ib class such as SN 2020qef Terreran et al. (2020) and the SLSN-I 2016wi Yan et al. (2017). We assign a Silver label due to the poor photometric coverage. Comparison spectra are from Piranomonte et al. (2019).

C.11. 2019wpb

SN 2019wpb (=ZTF19acxxxec = PS19heh) was classified as an SN Ic by Prentice et al. (2019d). We adopt a redshift of $z=0.06779$ from a spectrum of the host galaxy from the Sloan Digital Sky Survey (SDSS; Stoughton et al. 2002). The spectra match that of an SN Ic. We assign a Silver label since there is only one data point in ATLAS-c band during the rise.

C.12. 2021lei

SN 2021lei was classified as an SN Ic by Leloudas et al. (2021). We obtained spectra using the IMACS spectrograph, and include photometry from ZTF and ATLAS. We assign a Silver label due to the peculiar colors of the SN, which our model is not able to reproduce accurately.

C.13. iPTF13dnt

iPTF13dnt was classified as an SN Ic-BL by Taddia et al. (2019). We include photometry and spectra from Taddia et al. (2019). The spectrum is mostly flat but consistent with an SN Ic. The light curve is brighter and with a slower decline than normal SNe Ic. We assign a Silver label since this object lacks photometry before peak and only has one spectrum with very weak features.

C.14. OGLE15xl

OGLE15xl was classified as an unknown kind of SN by Le Breton et al. (2015), and as an SLSN-I by C. Inserra et al. (2022, in preparation). Only the OGLE *I* band is available. We determine a redshift of $z=0.198$ is a better fit to the host emission lines than the redshift reported by OGLE of $z=0.2$. The light curve is broad but dim for an SLSN-I. The spectra are a better match to SLSN-I than to SNe Ic. We obtain the comparison spectrum from WISeREP. We assign a Silver label since only a single datum of photometry is available.

C.15. PTF10iam

PTF10iam was classified by Arcavi et al. (2016) as an intermediate SN between SLSN-I and normal Type I SNe. The source has possible signatures of hydrogen, which is why we assign a Silver label. The spectra are blue and consistent with an SLSN-I, but dimmer than normal SLSN-I. We include photometry and spectra from Arcavi et al. (2016).

Appendix D
Bronze LSNe

D.1. 1992ar

SN 1992ar was classified as an SN Ic by Hamuy et al. (1992) and presented in Clocchiatti et al. (2000) as a luminous SN Ic. At the reported redshift of $z=0.145$ the peak magnitude of the SN is $M_V\sim-19$ mag, the most luminous for an SN Ic at the time, but not quite in the SLSN-I regime. We include photometry from Clocchiatti et al. (2000). We assign a Bronze label due to the lack of photometry during the rise or peak of the light curve, and overall very sparse light curve.

D.2. 2006jx

SN 2006jx (=SDSS-II SN 15170) was classified as a possible SN Ib at a redshift of $z=0.25$ by Bassett et al. (2006), but later reclassified as part of the SDSS-II Supernova Survey as an SN Ia at a redshift of $z=0.395$ by Sako et al. (2018). We include photometry from Sako et al. (2018). At the redshift of $z=0.395$ from Sako et al. (2018) the peak magnitude of the SN is $M_R\sim-20.4$, within the range of SLSN-I. We assign a Bronze label since there are no public spectra of the source and we are unable to confirm either classification.

D.3. 2007tx

SN 2007tx (=ESSENCEy122) was classified as an SN Ia by Silverman & Damke (2007) and later reclassified as an SN Ic at a redshift of $z=0.6764$ by Narayan et al. (2016). At this redshift, the peak absolute magnitude of the SN is uncertain but in the range of $M_R=-12.2\pm0.4$. We assign a Bronze label since there is only one public photometry datum of the source and the public spectrum has a very low S/N.

D.4. 2009bh

SN 2009bh (=PTF09q) was classified as a possible SLSN-I by Quimby et al. (2018) and as an SN Ic by Kasliwal et al. (2009). The peak absolute magnitude of $M_R \sim -18.6$ is well below the SLSN-I range but within the SNe Ic range. We assign a Bronze label since there is only one datum of photometry available.

D.5. 2009ca

SN 2009ca was originally classified as an SN Ic by Stritzinger et al. (2009) and then reclassified as an SN Ic-BL by Taddia et al. (2018), who point out the SN is significantly brighter than most SNe Ic-BL. We include photometry from Stritzinger et al. (2018) and some early photometry from Pignata et al. (2009). We assign a Bronze label since there are no photometry data points before or during peak and no public spectra of the source.

D.6. 2011cs

SN 2011cs (=CSS110427:120801+491333) was classified as an SN Ic by Drake et al. (2011). At the quoted redshift of $z = 0.1$, the peak magnitude of the SN is ~ -20 in an unfiltered C band. We include photometry from the CRTS. Nevertheless, we assign a Bronze label since there are no public spectra of the source and only unfiltered photometry available.

D.7. 2012gh

SN 2012gh (=CSS121026:164652+565105) was classified as an SN Ic by Tomasella et al. (2012). We include photometry from Mahabal et al. (2012) and one epoch from the CRTS. Most of the CRTS data is too uncertain to be reliable with high scatter. We do include upper limits from before and after peak from the CRTS. We assign a Bronze label since there are only two epochs of photometry available.

D.8. 2016gkm

SN 2016gkm (=Gaia16bjf = PS18jq = iPTF16gkm) was classified as an SN Ib/c by Galbany et al. (2019). We include photometry from PS1 and the GSA. We do not include existing photometry from the Cambridge Photometry Calibration Server (CPCS; Zieliński et al. 2019) since this appears highly discrepant. We assign a Bronze label due to the lack of good photometric coverage and no detections during or before the peak.

D.9. 2017dgk

SN 2017dgk was classified as an SN Ic at $z = 0.058$ by Gutierrez et al. (2017), but we find a better match to a redshift of $z = 0.065$ using narrow emission lines from the host galaxy. We include photometry from Cacella (2017). We assign a Bronze label since there is a single datum of photometry of the source, and this is in an unfiltered band with no quoted error bars.

D.10. 2017iwh

SN 2017iwh (=Gaia17dfz) was classified as an SN Ic by Angus et al. (2017). We include photometry from the GSA. We assign a Bronze label since there is no photometry coverage during the rise or peak and only single datum of photometry exists.

D.11. 2018hom

SN 2018hom (=ZTF18acbwxcc = Gaia18dfj = ATLAS18xyr) was classified as an SN Ic-BL by Fremling et al. (2018b). We include photometry from ZTF, the GSA, and ATLAS. We subtract a nominal $m_G = 18.07$ magnitude from the GSA photometry to account for the host flux, estimated from the average pre-explosion photometry. We adopt a redshift of $z = 0.0297$, from a spectrum of the host in the LEDA catalog (Makarov et al. 2014) as opposed to the redshift of $z = 0.0362$ reported by Fremling et al. (2018b). This new redshift makes it such that the source is no longer particularly bright or broad, but barely on the high margin for SNe Ic, hence the Bronze label.

D.12. 2019dgw

SN 2019dgw (=ZTF19aapwnmb) was classified as an SN Ib by Fremling et al. (2019c). We include our own PSF photometry from ZTF images after doing difference imaging to subtract the host flux. We assign a Bronze label since the light curve only has one datum of photometry during the rise, and the single available spectrum has low S/N and shows large broad features which could be artifacts.

D.13. PS110ahq

PS110ahq (=PSc080762) was classified as an SN Ic by McCrum et al. (2015). We include MDS photometry from Hosseinzadeh et al. (2020), Villar et al. (2020), excluding data before MJD = 55460, since those are from well before explosion. We assign a Bronze label given the lack of photometry before peak and lack of publicly available spectra. The SN also has a close resemblance to a normal SN Ic with a peak magnitude of $M_r = 19.2$ mag.

D.14. PTF10cs

PTF10cs was classified as an SN Ic-BL by Taddia et al. (2019). We include photometry from Taddia et al. (2019). We assign a Bronze label since there are only three public photometry data points of the source and no spectra available for download.

D.15. PTF11hrq

PTF11hrq was classified as an SLSN-I by Quimby et al. (2018). The host galaxy of PTF11hrq was studied by Perley et al. (2016), who found a redshift of $z = 0.057$. We include photometry from De Cia et al. (2018), which the authors correct for extinction using $E(B-V) = 0.013$. There are no early spectra available, which makes distinguishing between SLSN-I and SNe Ic spectra challenging. We assign a Bronze label since there is no photometry during the rise or peak of the SN. Our `MOSFiT` model predicts a peak magnitude between that of SLSN-I and SNe Ic.

D.16. PTF12grr

PTF12grr was classified as an SN Ic-BL by Taddia et al. (2019). We include photometry from Taddia et al. (2019). We assign a Bronze label due to the very poor light-curve coverage and the fact there are no spectra of the source available for download.

D.17. SNLS04D4ec

SNLS04D4ec was classified by Arcavi et al. (2016) as an intermediate supernova between SLSN-I and normal Type I

SNe. Nevertheless, we assign a Bronze label since there are no spectra of the source during peak, but only of the host galaxy. We only include photometry from Arcavi et al. (2016).

D.18. SNLS05D2bk

SNLS05D2bk was classified by Arcavi et al. (2016) as an intermediate supernova between SLSN-I and normal Type I SNe. Nevertheless, we assign a Bronze label since there are no spectra of the source during peak, but only of the host galaxy. We only include photometry from Arcavi et al. (2016).

D.19. SNLS06D1hc

SNLS06D1hc was classified by Arcavi et al. (2016) as an intermediate supernova between SLSN-I and normal Type I SNe. Nevertheless, we assign a Bronze label since there are no spectra of the source during peak, but only of the host galaxy. We only include photometry from Arcavi et al. (2016).

Appendix E
Excluded LSNe

These objects were excluded from our sample since they have been well studied before and appear to be very different in nature from the LSNe population.

E.1. 1998bw

SN 1998bw (=GRB980425A = AAVSO 1927-53) was classified as a luminous SNe Ic-BL with an associated GRB by Galama et al. (1998), Wang & Wheeler (1998), and Kulkarni et al. (1998). We exclude this object from our sample because even though SN 1998bw passes the threshold for having a luminosity in between that of SNe Ic and SLSNe, this is a well-known luminous SNe Ic-BL with very broad spectral features and significantly different from any SN in the LSNe sample.

E.2. 2018gep

SN 2018gep (=ZTF18abukavn = ATLAS18vah) was classified as an SN Ic-BL by Burke et al. (2018) and presented in Ho et al. (2019). We exclude this object from our sample since it was thoroughly studied in Ho et al. (2019) and appears to be a peculiar transient with different photometric and spectroscopic features to the sample presented here, related to fast transients such as AT 2018cow more than LSNe.

E.3. ASASSN-15no

ASASSN-15no was presented in Benetti et al. (2018) as an SN with features of SLSN-I, normal SNe Ib/c, but also signs of interaction, such as hydrogen emission lines. The spectral data are not available for download, but visual inspection suggests the spectrum is roughly consistent with an SLSN-I. The peak luminosity and decline rate are between those of SLSN-I and SNe Ic. We exclude this object since Benetti et al. (2018) explored it in detail revealing this SN to be very different in nature to the sample presented here, with signs on interaction.

E.4. 2021lji

SN 2021lji was classified as an SLSN-I by Charalampopoulos et al. (2021), who determine a redshift of $z = 0.12$ from the SN features. We obtained a late-time spectrum with the Binospec spectrograph that shows clear host emission lines, from which we derive a redshift of $z = 0.092$. We exclude this object from our sample since the new redshift means it matches a normal CCSN.

Appendix F
Comparison SNe

We include a sample of SNe Ic and SNe Ic-BL for comparison with our sample of LSNe.

We include the SNe Ic-BL iPTF13ebw, iPTF13u, iPTF14dby, iPTF14gaq, iPTF16gox, iPTF17axg, iPTF16ilj, PTF10aavz, PTF10ciw, PTF10qts, PTF10tqv, PTF10vgv, PTF10xem, PTF11cmh, PTF11lbm, PTF12as, PTF12eci, and iPTF16coi from Taddia et al. (2019). For iPTF13u we exclude the single *B*-band data point due to its high discrepancy from the rest of the data.

We include the SNe Ib/c PTF09dh, PTF09ut, PTF10bip, PTF10lbo, PTF10osn, PTF10tqi, PTF10yow, PTF10zcn, PTF11bli, PTF11bov, PTF11hyg, PTF11jgj, PTF11klg, PTF11lmn, PTF11mwk, PTF11rka, PTF12dtf, PTF12dcp, PTF12cjy, PTF12fgw, PTF12hvv, PTF12jxd, PTF12ktu, PTF13ab, PTF13aot, PTF13cuv, PTF13dht, PTF13djf, PTF14gao, PTF14gqr, PTF14fuz, PTF14jhf, PTF14ym, PTF15acp, PTF15cpq, PTF15dtg, PTF16flq, and PTF16hgp from Barbarino et al. (2020).

We also include the entire samples of SLSNe from Nicholl et al. (2017), Villar et al. (2018), Blanchard et al. (2020), Gomez et al. (2020a) and newer SLSNe that will be presented in S. Gomez et al. (2022, in preparation): 2002gh, 2005ap, 2006oz, 2007bi, 2009jh, 2010gx, 2010hy, 2010kd, 2010md, 2011ke, 2011 kg, 2012il, 2013dg, 2015bn, 2016aj, 2016ard, 2016eay, 2016inl, 2016wi, 2017beq, 2017dwh, 2017egm, 2017ens, 2017gci, 2017jan, 2018avk, 2018bgv, 2018bsz, 2018bym, 2018cxa, 2018fd, 2018ffj, 2018ffs, 2018gkz, 2018hti, 2018ibb, 2018kyt, 2018lfe, 2019cca, 2019cdt, 2019cwu, 2019dlr, 2019eot, 2019gam, 2019gfm, 2019gqi, 2019hge, 2019hno, 2019itq, 2019kcy, 2019kwq, 2019kws, 2019kwt, 2019kwu, 2019lsq, 2019neq, 2019nhs, 2019obk, 2019pud, 2019sgh, 2019szu, 2019ujb, 2019unb, 2019xaq, 2019zbv, 2019zeu, 2020abjc, 2020adkm, 2020ank, 2020exj, 2020jii, 2020onb, 2020qef, 2020qlb, 2020rmv, 2020uew, 2020xga, 2020xgd, 2020znr, 2020zzb, 2021bnw, 2021een, 2021ejo, 2021ek, 2021fpl, 2021gtr, 2021hpc, 2021hpx, 2021mkr, 2021nxq, 2021txk, 2021vuw, 2021xfu, 2021yrp, 2021zcl, CSS160710, DES14S2qri, DES14X2byo, DES14X3taz, DES15E2mlf, DES15X1noe, DES15X3hm, DES16C2aix, DES16C2nm, DES16C3dmp, DES16C3ggu, DES17X1amf, DES17X1blv, iPTF13ajg, iPTF13dcc, iPTF13ehe, iPTF16bad, iPTF16eh, LSQ12dlf, LSQ14an, LSQ14bdq, LSQ14fxj, LSQ14mo, OGLE15qz, OGLE15sd, OGLE15xx, OGLE16dmu, PS110awh, PS110bzj, PS110ky, PS110pm, PS111afv, PS111aib, PS111ap, PS111bam, PS111bdn, PS112bqf, PS112cil, PS113or, PS114bj, PS15cjz, PTF09atu, PTF09cnd, PTF10aagc, PTF10bfz, PTF10nmn, PTF10uhf, PTF10vqv, PTF12dam, PTF12mxx, SCP06F6, SNLS06D4eu, SNLS07D2bv, and SSS120810.

Appendix G
Individual Light Curves

We include light curve plots for all bands in Figure 17 and corner plots in Figure 18 for the models of all 40 LSNe.

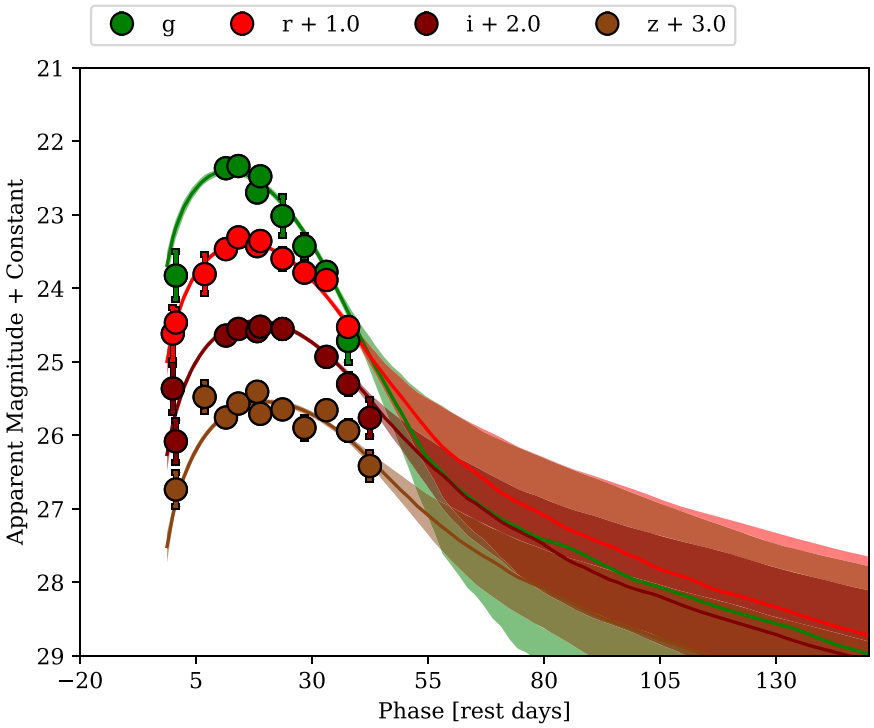

Figure 17. Example light curve for DES14C1rhg. The complete figure set (40 images) is available in the online journal. (The complete figure set (40 images) is available.)

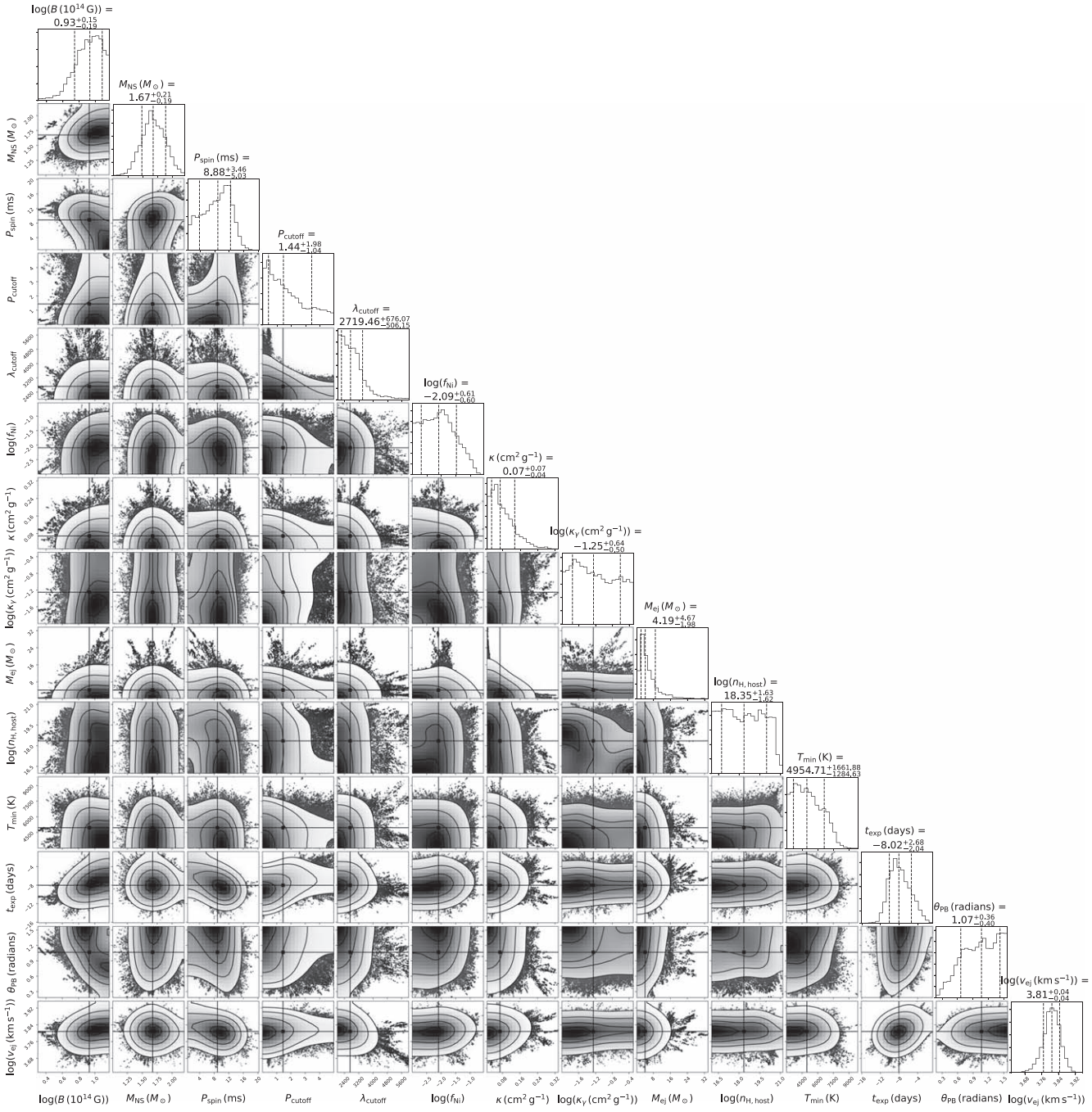

Figure 18. Corner plots for DES14C1rhg. The complete figure set (40 images) is available in the online journal.
(The complete figure set (40 images) is available.)

Appendix H
Individual Corner Plots

We include light curve plots for all bands in Figure 17 and corner plots in Figure 18 for the models of all 40 LSNe.

ORCID iDs

Sebastian Gomez https://orcid.org/0000-0001-6395-6702
Edo Berger https://orcid.org/0000-0002-9392-9681
Matt Nicholl https://orcid.org/0000-0002-2555-3192
Peter K. Blanchard https://orcid.org/0000-0003-0526-2248
Griffin Hosseinzadeh https://orcid.org/0000-0002-0832-2974

References

Afsariardchi, N., Drout, M. R., Khatami, D. K., et al. 2021, ApJ, 918, 89
Anderson, J. P. 2019, A&A, 628, A7
Angus, C. R., Angus, C. R., Frohmaier, C., Yaron, O., & Knezevic, N. 2017, TNSCR, 2017-1407, 1
Angus, C. R., Levan, A. J., Perley, D. A., et al. 2016, MNRAS, 458, 84
Angus, C. R., Smith, M., Sullivan, M., et al. 2019, MNRAS, 487, 2215
Arcavi, I., Wolf, W. M., Howell, D. A., et al. 2016, ApJ, 819, 35

Arnett, W. D. 1982, ApJ, 253, 785
Astropy Collaboration, Price-Whelan, A. M., Sipőcz, B. M., et al. 2018, AJ, 156, 123
Barbarino, C., Sollerman, J., Taddia, F., et al. 2020, arXiv:2010.08392
Barbary, K. 2016, Extinction V0.3.0, Zenodo, doi:10.5281/zenodo.804967
Bassett, B., Becker, A., Brewington, H., et al. 2006, CBET, 680, 1
Becker, A. 2015, HOTPANTS: High Order Transform of PSF ANd Template Subtraction, Astrophysics Source Code Library, ascl:1504.004
Bellm, E. C., Kulkarni, S. R., Graham, M. J., et al. 2019, PASP, 131, 018002
Benetti, S., Branch, D., Turatto, M., et al. 2002, MNRAS, 336, 91
Benetti, S., Zampieri, L., Pastorello, A., et al. 2018, MNRAS, 476, 261
Bianco, F. B., Modjaz, M., Hicken, M., et al. 2014, ApJS, 213, 19
Blanchard, P. K., Berger, E., Nicholl, M., & Villar, V. A. 2020, ApJ, 897, 114
Blanchard, P. K., Nicholl, M., Berger, E., et al. 2019, ApJ, 872, 90
Brown, T. M., Baliber, N., Bianco, F. B., et al. 2013, PASP, 125, 1031
Bruch, R., Anderson, J., Gutierrez, C., & Irani, I. 2021, TNSCR, 2021-3392, 1
Burke, J., Arcavi, I., Hiramatsu, D., et al. 2018, TNSCR, 2018-1442, 1
Cacella, P. 2017, TNSTR, 2017-464, 1
Cardelli, J. A., Clayton, G. C., & Mathis, J. S. 1989, ApJ, 345, 245
Chambers, K. C., Magnier, E. A., Metcalfe, N., et al. 2016, arXiv:1612.05560
Charalampopoulos, P., Pursiainen, M., Leloudas, G., Paraskeva, E., & Zimmerman, E. 2021, TNSCR, 2021-1783, 1
Chatzopoulos, E., Wheeler, J. C., Vinko, J., Horvath, Z. L., & Nagy, A. 2013, ApJ, 773, 76
Chen, Z. H., Yan, L., Kangas, T., et al. 2022, arXiv:2202.02059
Chevalier, R. A., & Irwin, C. M. 2011, ApJL, 729, L6
Chomiuk, L., Chornock, R., Soderberg, A. M., et al. 2011, ApJ, 743, 114
Chu, M., Dahiwale, A., & Fremling, C. 2021, TNSCR, 2021-3171, 1
Clocchiatti, A., Phillips, M. M., Suntzeff, N. B., et al. 2000, ApJ, 529, 661
Dahiwale, A., Dugas, A., & Fremling, C. 2019a, TNSCR, 2019-2859, 1
Dahiwale, A., Dugas, A., & Fremling, C. 2019b, TNSCR, 2019-1505, 1
Dahiwale, A., & Fremling, C. 2020a, TNSCR, 2020-1667, 1
Dahiwale, A., & Fremling, C. 2020b, TNSCR, 2020-1504, 1
De Cia, A., Gal-Yam, A., Rubin, A., et al. 2018, ApJ, 860, 100
Dessart, L., Hillier, D. J., Waldman, R., Livne, E., & Blondin, S. 2012, MNRAS Lett., 426, L76
Dessart, L., Hillier, D. J., Woosley, S., et al. 2016, MNRAS, 458, 1618
Drake, A. J., Djorgovski, S. G., Mahabal, A., et al. 2009, ApJ, 696, 870
Drake, A. J., Djorgovski, S. G., Mahabal, A., et al. 2011, CBET, 2733, 2
Dressler, A., Bigelow, B., Hare, T., et al. 2011, PASP, 123, 288
Ertl, T., Woosley, S. E., Sukhbold, T., & Janka, H. T. 2020, ApJ, 890, 51
Fabricant, D., Fata, R., Epps, H., et al. 2019, PASP, 131, 075004
Filippenko, A. V. 1997, ARA&A, 35, 309
Foreman-Mackey, D. 2016, JOSS, 1, 24
Foreman-Mackey, D., Hogg, D. W., Lang, D., & Goodman, J. 2013, PASP, 125, 306
Förster, F., Cabrera-Vives, G., Castillo-Navarrete, E., et al. 2021, AJ, 161, 242
Fremling, C., Dugas, A., & Sharma, Y. 2018a, TNSCR, 2018-1232, 1
Fremling, C., Dugas, A., & Sharma, Y. 2018b, TNSCR, 2018-1720, 1
Fremling, C., Dugas, A., & Sharma, Y. 2019a, TNSCR, 2019-2797, 1
Fremling, C., Dugas, A., & Sharma, Y. 2019b, TNSCR, 2019-747, 1
Fremling, C., Dugas, A., & Sharma, Y. 2019c, TNSCR, 2019-733, 1
Fremling, C., Dugas, A., & Sharma, Y. 2019d, TNSCR, 2019-799, 1
Fremling, C., Sharma, Y., & Dahiwale, A. 2019e, TNSCR, 2019-1838, 1
Frohmaier, C., Angus, C. R., Vincenzi, M., et al. 2021, MNRAS, 500, 5142
Galama, T. J., Vreeswijk, P. M., van Paradijs, J., et al. 1998, Natur, 395, 670
Galbany, L., Badenes, C., Law, D., & Gelfand, J. D. 2019, TNSCR, 2019-1236, 1
Gal-Yam, A. 2017, Observational and Physical Classification of Supernovae (New York: Springer), 195
Gal-Yam, A. 2019, ARA&A, 57, 305
Gelman, A., Hwang, J., & Vehtari, A. 2014, Stat. Comput., 24, 997
Gelman, A., & Rubin, D. B. 1992, StaSc, 7, 457
Gomez, S., Berger, E., Blanchard, P. K., et al. 2020a, ApJ, 904, 74
Gomez, S., Berger, E., Blanchard, P. K., et al. 2020b, FLEET Finding Luminous and Exotic Extragalactic Transients, v1.0.0, Zenodo, doi:10.5281/zenodo.4013965
Gomez, S., Berger, E., Hosseinzadeh, G., et al. 2021, ApJ, 913, 143
Gomez, S., Berger, E., Nicholl, M., et al. 2019, ApJ, 881, 87
Gomez, S., Hosseinzadeh, G., Berger, E., & Blanchard, P. 2021, TNSCR, 2021-565, 1
Greiner, J., Mazzali, P. A., Kann, D. A., et al. 2015, Natur, 523, 189
Guillochon, J., Nicholl, M., Villar, V. A., et al. 2018, ApJS, 236, 6
Guillochon, J., Parrent, J., Kelley, L. Z., & Margutti, R. 2017, ApJ, 835, 64
Gutierrez, C., Cartier, R., & Yaron, O. 2017, TNSCR, 2017-474, 1
Hamuy, M., Maza, J., Antezana, R., et al. 1992, IAUC, 5574, 1
Heger, A., Fryer, C. L., Woosley, S. E., Langer, N., & Hartmann, D. H. 2003, ApJ, 591, 288
Hernandez-Garcia, A., Garcia-Zamora, E. M., Mallorquin, M., et al. 2018, ATel, 12341, 1
Hinshaw, G., Larson, D., Komatsu, E., et al. 2013, ApJS, 208, 19
Ho, A. Y. Q., Goldstein, D. A., Schulze, S., et al. 2019, ApJ, 887, 169
Hosseinzadeh, G., Dauphin, F., Villar, V. A., et al. 2020, ApJ, 905, 93
Hsu, B., Hosseinzadeh, G., & Berger, E. 2021, ApJ, 921, 180
Huber, M., Chambers, K. C., Flewelling, H., et al. 2015, ATel, 7153, 1
Hunter, J. D. 2007, CSE, 9, 90
Jerkstrand, A., Fransson, C., Maguire, K., et al. 2012, A&A, 546, A28
Jerkstrand, A., Smartt, S. J., Inserra, C., et al. 2017, ApJ, 835, 13
Ivezić, Ž., Kahn, S. M., Tyson, J. A., et al. 2019, ApJ, 873, 111
Kangas, T., Dennefeld, M., Harmanen, J., et al. 2015, ATel, 8296, 1
Kann, D. A., Schady, P., Olivares, E. F., et al. 2019, A&A, 624, A143
Kasen, D., & Bildsten, L. 2010, ApJ, 717, 245
Kasliwal, M. M., Quimby, R., Nugent, P., et al. 2009, CBET, 1732, 1
Khatami, D. K., & Kasen, D. N. 2019, ApJ, 878, 56
Kochanek, C. S., Shappee, B. J., Stanek, K. Z., et al. 2017, PASP, 129, 104502
Könyves-Tóth, R., & Vinkó, J. 2021, ApJ, 909, 24
Kulkarni, S. R., Frail, D. A., Wieringa, M. H., et al. 1998, Natur, 395, 663
Le Breton, R., Le Guillou, L., Fraser, M., et al. 2015, ATel, 8437, 1
Leloudas, G., Irani, D. B. M., Pursiainen, M., Charalampopoulos, P., & Yaron, O. 2021, TNSCR, 2021-1606, 1
Liu, J.-F., Zhu, J.-P., Liu, L.-D., Yu, Y.-W., & Zhang, B. 2022, ApJL, 935, L34
Lunnan, R., Chornock, R., Berger, E., et al. 2014, ApJ, 787, 138
Lunnan, R., Yan, L., Fremling, C., et al. 2018, ATel, 11986, 1
Lunnan, R., Yan, L., Perley, D. A., et al. 2020, ApJ, 901, 61
Mahabal, A. A., Drake, A. J., Djorgovski, S. G., et al. 2012, CBET, 3297, 1
Makarov, D., Prugniel, P., Terekhova, N., Courtois, H., & Vauglin, I. 2014, A&A, 570, A13
Margalit, B., Metzger, B. D., Berger, E., et al. 2018, MNRAS, 481, 2407
Matheson, T., Filippenko, A. V., Li, W., Leonard, D. C., & Shields, J. C. 2001, AJ, 121, 1648
Maza, J., & Ruiz, M. T. 1989, ApJS, 69, 353
Mazzali, P. A., & Lucy, L. B. 1993, A&A, 279, 447
Mazzali, P. A., McFadyen, A. I., Woosley, S. E., Pian, E., & Tanaka, M. 2014, MNRAS, 443, 67
Mazzali, P. A., Sullivan, M., Pian, E., Greiner, J., & Kann, D. A. 2016, MNRAS, 458, 3455
Mcbrien, O., Clark, P., Kankare, E., Yaron, O., & Knezevic, N. 2018, TNSCR, 2018-587, 1
McCrum, M., Smartt, S. J., Rest, A., et al. 2015, MNRAS, 448, 1206
Metzger, B. D., Margalit, B., Kasen, D., & Quataert, E. 2015, MNRAS, 454, 3311
Milisavljevic, D., Soderberg, A. M., Margutti, R., et al. 2013, ApJL, 770, L38
Modjaz, M., Bianco, F. B., Siwek, M., et al. 2020, ApJ, 892, 153
Modjaz, M., Blondin, S., Kirshner, R. P., et al. 2014, AJ, 147, 99
Nadyozhin, D. K. 1994, ApJS, 92, 527
Narayan, G., Rest, A., Tucker, B. E., et al. 2016, ApJS, 224, 3
Nicholl, M., Berger, E., Blanchard, P. K., Gomez, S., & Chornock, R. 2019, ApJ, 871, 102
Nicholl, M., Guillochon, J., & Berger, E. 2017, ApJ, 850, 55
Nicholl, M., Short, P., Lawrence, A., Ross, N., & Smartt, S. 2019, TNSAN, 68, 1
Nicholl, M., Smartt, S. J., Jerkstrand, A., et al. 2015, MNRAS, 452, 3869
Nogami, D., Kato, T., Baba, H., & Kunjaya, C. 1997, in Electronic Publishing, Now and the Future, 23rd Meet. of the IAU, Jt. Discuss. 12 (Kyoto, Japan: Electronic Publishing), 2
Ouyed, R., Leahy, D., & Koning, N. 2015, ApJ, 809, 142
Özel, F., & Freire, P. 2016, ARA&A, 54, 401
Papadopoulos, A., D'Andrea, C. B., Sullivan, M., et al. 2015, MNRAS, 449, 1215
Pastorello, A., Smartt, S. J., Botticella, M. T., et al. 2010, ApJL, 724, L16
Perley, D. A., Fremling, C., Sollerman, J., et al. 2020, ApJ, 904, 35
Perley, D. A., Quimby, R. M., Yan, L., et al. 2016, ApJ, 830, 13
Perley, D. A., Yao, Y., Chen, T., et al. 2021, TNSCR, 2021-1649, 1
Pignata, G., Maza, J., Hamuy, M., et al. 2009, CBET, 1750, 1
Piranomonte, S., Carini, R., Melandri, A., D'avanzo, P., & Yaron, O. 2019, TNSCR, 2019-159, 1
Poidevin, F., Perez-Fournon, I., Angel, C. J., et al. 2021, TNSCR, 2021-2800, 1
Prentice, S. J., Inserra, C., Schulze, S., et al. 2021, MNRAS, 508, 4342
Prentice, S. J., Maguire, K., Skillen, K., Magee, M. R., & Clark, P. 2019a, TNSCR, 2019-2339, 1

Prentice, S. J., Maguire, K., Skillen, K., Magee, M. R., & Clark, P. 2019b, TNSCR, 2019-625, 1
Prentice, S. J., Maguire, K., Skillen, K., Magee, M. R., & Clark, P. 2019c, TNSCR, 2019-1598, 1
Prentice, S. J., Maguire, K., Skillen, K., Magee, M. R., & Clark, P. 2019d, TNSCR, 2019-2723, 1
Quimby, R., Odewahn, S. C., Terrazas, E., Rau, A., & Ofek, E. O. 2007, CBET, 953, 1
Quimby, R. M., De Cia, A., Gal-Yam, A., et al. 2018, ApJ, 855, 2
Quimby, R. M., Kulkarni, S. R., Kasliwal, M. M., et al. 2011, Natur, 474, 487
Ridley, E., Gompertz, B., Nicholl, M., Galbany, L., & Yaron, O. 2021, TNSCR, 2021-2795, 1
Roy, R., Sollerman, J., Silverman, J. M., et al. 2016, A&A, 596, A67
Sako, M., Bassett, B., Becker, A. C., et al. 2018, PASP, 130, 064002
Sanders, N. E., Soderberg, A. M., Valenti, S., et al. 2012, ApJ, 756, 184
Schlafly, E. F., & Finkbeiner, D. P. 2011, ApJ, 737, 103
Schmidt, G. D., Weymann, R. J., & Foltz, C. B. 1989, PASP, 101, 713
Science Software Branch at STScI 2012, PyRAF: Python Alternative for IRAF, Astrophysics Source Code Library, ascl:1207.011
Shivvers, I., Filippenko, A. V., Silverman, J. M., et al. 2019, MNRAS, 482, 1545
Silverman, J. M., & Damke, G. 2007, CBET, 1186, 2
Smith, N. 2014, ARA&A, 52, 487
Smithsonian Astrophysical Observatory 2000, SAOImage DS9: A Utility for Displaying Astronomical Images in the X11 Window Environment, Astrophysics Source Code Library, ascl:0003.002
Soderberg, A. M., Kulkarni, S. R., Berger, E., et al. 2005, ApJ, 621, 908
Soker, N., & Gilkis, A. 2017, ApJ, 851, 95
Stevenson, K. B., Bean, J. L., Seifahrt, A., et al. 2016, ApJ, 817, 141
Stoughton, C., Lupton, R. H., Bernardi, M., et al. 2002, AJ, 123, 485
Stritzinger, M., Mazzali, P., Phillips, M. M., et al. 2009, ApJ, 696, 713
Stritzinger, M. D., Anderson, J. P., Contreras, C., et al. 2018, A&A, 609, A134
Taddia, F., Sollerman, J., Fremling, C., et al. 2019, A&A, 621, A71
Taddia, F., Stritzinger, M. D., Bersten, M., et al. 2018, A&A, 609, A136
Taggart, K., & Perley, D. 2021, MNRAS, 503, 3931
Terreran, G., Blanchard, P., DeMarchi, L., et al. 2020, ATel, 13970, 1
Tomasella, L., Benetti, S., Cappellaro, E., et al. 2012, ATel, 4548, 1
Tonry, J. L., Denneau, L., Heinze, A. N., et al. 2018, PASP, 130, 064505
Valenti, S., Cappellaro, E., Danese, S., et al. 2003, IAUC, 8057, 2
van der Walt, S., Colbert, S. C., & Varoquaux, G. 2011, CSE, 13, 22
Villar, V. A., Hosseinzadeh, G., Berger, E., et al. 2020, ApJ, 905, 94
Villar, V. A., Nicholl, M., & Berger, E. 2018, ApJ, 869, 166
Wang, L., & Wheeler, J. C. 1998, ApJL, 504, L87
Watanabe, S. 2010, J. Mach. Learn. Res., 11, 3571
Whitesides, L., Lunnan, R., Kasliwal, M. M., et al. 2017, ApJ, 851, 107
Woosley, S. E. 2010, ApJL, 719, L204
Woosley, S. E., Blinnikov, S., & Heger, A. 2007, Natur, 450, 390
Woosley, S. E., Langer, N., & Weaver, T. A. 1995, ApJ, 448, 315
Wyrzykowsk, Ł. 2016, in 37th Meet. Polish Astron. Soc. Vol. 3, ed. A. Różańska & M. Bejger (Warsaw, Poland: Polish Astronomical Society), 65
Wyrzykowski, Ł., Kostrzewa-Rutkowska, Z., Kozłowski, S., et al. 2014, AcA, 64, 197
Yan, L., Lunnan, R., Perley, D. A., et al. 2017, ApJ, 848, 6
Yan, L., Perley, D., Schulze, S., et al. 2020, TNSCR, 2020-1737, 1
Yan, L., Perley, D. A., De Cia, A., et al. 2018, ApJ, 858, 91
Yan, L., Perley, D. A., Schulze, S., et al. 2020, ApJL, 902, L8
Yan, L., Quimby, R., Ofek, E., et al. 2015, ApJ, 814, 108
Yaron, O., & Gal-Yam, A. 2012, PASP, 124, 668
Zieliński, P., Wyrzykowski, Ł., Rybicki, K., et al. 2019, CoSka, 49, 125